A Fourdimensional Microscope for Single Molecule Studies in Living Cells Using Astigmatic Axial Resolution Enhancement

Erik Hedlund

A thesis submitted in partial fulfilment of the requirements for the degree of Master of Science by Research at the University of Oxford
Wolfson College, University of Oxford Trinity Term 2015

Disclaimer

I hereby declare that the work in this thesis is that of the candidate alone, except where indicated in the text, and as described below.

• The PSF finding software is based on code developed by Isabel Llorente Garcia.

• The Gaussian fitting software is based on software developed by Gero Nootz. A detailed copyright disclaimer is included in appendix B as required by the licensing terms

• Samples of YPet tagged Escherichia Coli was kindly provided by Oliver Harriman.

Erik Hedlund October 2015

A Fourdimensional Microscope for Single Molecule Studies in Living Cells Using Astigmatic Axial Resolution Enhancement

Erik Hedlund, Wolfson College

A thesis submitted for the degree of Master of Science by Research
at the University of Oxford, Trinity Term 2015

Abstract

An important part of life is to react to the environment and adapt to it. All living cells rely on chemical cascades that form signal pathways, from stimulus to transcription events at the DNA. To know more about these pathways we need tools to visualise the signals.

Here is outlined developmental and experimental work on a bespoke microscope system primarily for fast single molecule tracing of proteins in living eukaryote cells. Both hardware and software has been developed. Frame rates and exposure times have been pushed to match the speed of freely diffusing particles in living cells. An EMCCD camera with an electronic gain of 300x and a 5 ms exposure time at 200 frames per second enables this.

An astigmatic axial resolution enhancement approach has been implemented to allow tracking with high precision of single fluorescent proteins in real-time in three dimensions in a comparatively large volume. The high resolution in three spatial dimensions and one temporal aim to meet these demands. Software to extract the additional axial information has been developed that can determine axial displacement with 38 nm precision.

The microscope system has proven it can find and track small clusters of YPet fluorescent protein in *E. coli* at short exposure times.

Acknowledgements

I would like to thank all the forces having worked together to put me where I am today.

A big Thank you to Mark, my supervisor for believing in me and inspiring me.

All my love to Diana, my lovely wife for always kicking on the right spots on my behind, forcing me forward when things do not work the way I want them to.

And finally the European Commission for the opportunity presented to me to study biological physics under the supervision of Mark Leake in Oxford and subsequently in York as a *Marie Curie Actions early stage researcher*.



ISOLATE

ISOLATE is an Initial Training Network funded and supervised by the European Union 7th Framework Programme. Grant agreement number: 289995. The Network is coordinated at Göteborgs Universitet in Gothenburg, Sweden. The network has five university nodes and two commercial partners. Each of the different nodes has a different focus with the same overarching objective, to study molecular systems biology at the single cell and single molecule scale.

In Gothenburg in Sweden and at the Rijksuniversiteit van Groningen in the Netherlands work is conducted on *Saccharomyces cerevisiæ,* including specialised genetic modifications instrumental to the investigations conducted at the UK node.

The purpose of the UK node is to develop novel microscopy methods to push the limit of modern imaging of living cells and their function in a complex biological setting (ref: ISOLATE documents). The British node was initially located at the University of Oxford and this is where the system laid out in this document was primarily realised. The UK node has since relocated to the University of York.

Contents

1 Introduction....8

2 IMAGING LIVING CELLS....13

3 MICROSCOPY....16

4 SUPER-RESOLUTION TECHNIQUES....24

5 CHARACTERISATION....32

5.1 PREPARATION OF FLOW CHANNELS FOR BEADS....32

5.2 DATA FROM LIVING CELLS....33

6 SOFTWARE DESIGN....35

6.1 CONSIDERATIONS....39

7 DATA ANALYSIS....40

8 CONCLUSIONS AND FUTURE DEVELOPMENT....53

A. APPENDIX: SOFTWARE FLOWCHARTS (SOURCE CODE)....55

B. MANDATORY SOFTWARE LICENSE ACKNOWLEDGEMENTS....58

BIBLIOGRAPHY....60

List of abbreviations and protein names

Cerulean	A fluorescent protein
DH-PSF	Double Helix Point Spread Function
FP	Fluorescent Protein
FWHM	Full Width at Half Maximum
GUI	Graphical User Interface
LB	Lysogeny Broth
mCherry	A red fluorescent protein
mPlum	A fluorescent protein
OD_{600nm}	Optical Density at 600 nm
(F)PALM	(Fluorescence) Photo-Activated Localisation Microscopy
PSF	Point Spread Function
ROI	Region Of Interest
SLM	Spatial Light Modulator
STORM	STochastic Optical Reconstruction Microscopy
YFP	Yellow Fluorescent Protein (sometimes called YGFP)
YPet	A type of yellow fluorescent protein

INTRODUCTION

The aim of this project has been to develop and characterise a microscope system capable of visualising and locating single fluorophores – single proteins within living cells. Specifically targeted are *Saccharomyces cerevisiæ* cells and to do this precisely in the three spatial dimensions, in two emission wavelength bands and with high temporal resolution. The main challenges to overcome in order to accomplish this are to improve the spatial axial resolution and to improve the temporal resolution, i.e. achieve short camera exposure times whilst still being able to image down to single molecules of fluorophores as dim as fluorescent proteins. Michalet and Weiss explored the possibilities of single molecule microscopy with regards to signal to noise requirements and technical options in 2002 (Michalet & Weiss 2002), using a near-field scanning technique.

The in-plane resolution of a microscope using a wide-field configuration is determined by several factors, most important of which being the numerical aperture of the objective lens and also the wavelength at which the sample is imaged. If the aim is to image single molecules also the sparsity of fluorophores is an important factor as due to what is known as the Rayleigh criterion, a point source cannot be discerned from another, adjacent point source if the two are too close to each other (Fischer et al. 2008; Webb 1996; Wegerhoff et al. 2007). But if any point sources imaged are sufficiently well separated, it is possible to find their lateral position to a very high precision. This is one of the main working principles behind finding the lateral locations of fluorophores in many modern super-resolution techniques such as Stochastic Optical Reconstruction Microscopy (STORM) and (Fluorescence) Photo-Activated Localisation Microscopy ((F)PALM) (Betzig et al. 2006; Huang et al. 2008). A more difficult task is to precisely pinpoint the axial position of sources that are in or

outside the immediate focal plane. As the aim is to ultimately image single molecules diffusing within yeast, this will prove important as yeast cells are fairly large organisms at around 5 microns across with even the nucleus being around a micron in diameter. These are distances significantly larger than the depth of field of a high magnification microscope in a wide-field configuration. This will be further discussed later.

Several techniques have been proposed to improve the resolution in the third dimension. To some extent these methods are assuming that the fluorophores will stay stationary or that exposure times can be kept sufficiently short for diffusing particles not to blur the image. The precision of the aforementioned methods, STORM and (F)PALM, can be further augmented in the axial dimension using various tricks on the emission side. In 2010 Majid Badieirostami summarised the performance of three methods, Astigmatism, Double-Helix PSF and Biplane imaging (Badieirostami et al. 2010). Of these, two were primarily considered for use in this project.

The techniques that were considered are:

- Emission side astigmatism – An aspherical element in the imaging beampath introduces an asymmetry that deforms the image of the point source in a distinct way depending on its distance from the focal plane. This is due to the focal plane along one of the lateral axes is shifted ever so slightly.

  The technique was described by Pin Kao and Verkman in 1994 (Kao & Verkman 1994) and was used by Bo Huang in 2008 when it was used in a superresolution STORM setting (Huang et al. 2008).

- Bespoke PSF shaping – Manipulating the appearance of the PSF on the detector by introducing a well-defined phase shift pattern in the Fourier plane of the imaging system. The seminal example is arguably the Double

Helix Point Spread Function (DH-PSF) technique described by Pavani & al. (Pavani & Piestun 2008; Pavani et al. 2009)

Later developments include e.g. Cork-screw PSF (Lew et al. 2011) based on similar theories and hardware solutions, using phase plates or spatial light modulators in the emission path Fourier plane.

Both these methods are in some sense Point Spread Function (PSF) shaping techniques that introduce some defocussing dependent perturbation of the image before being projected on the sensor. A deterministic behaviour of the image deformation can be used to determine the axial displacement of a point source within given constraints.

The astigmatism method can be considered a variant of the final method, Biplane imaging, mentioned by Badieirostami, as it also relies on offset imaging planes. Biplane imaging uses a (non-polarising) beam splitter to separate the image into two separate beampaths with slightly offset image planes (Juette et al. 2008). However, this method was never considered, as it would involve projecting a second image, either on the same camera, or on a second camera. The fact that the image is already split on the camera due to the colour splitting would make this option complicated to implement.

The base components of the system used in this project are a microscope body from Nikon and homemade bespoke excitation and imaging modules. The body is arranged in a configuration that allows for both bright-field dia-illumination and epi-fluorescence microscopy. Using standard components helps to make sure that the entirety of the beampaths from excitation light source to sample and from sample to image sensor are well defined. As excitation source was chosen a range of compact diode pumped solid-state laser systems from OBIS and Coherent. The compact form

factor facilitated the construction of standardised modules, built on 300 by 400 mm optical breadboards.

One main consideration has been to make the system portable. The modular design is one part of accomplishing this.

To control the microscope system, bespoke software was developed. Several control and data channels were integrated in one unified user interface. The controls include laser emission; sample position adjusted by a nano-piezo stage and camera operations.

The biological samples that are to be imaged by the system are quite sensitive to large light doses. Fluorescent proteins, introduced into cells for use as tags on certain proteins in order to pinpoint their position and interactions within, bleach very quickly. Any one fluorescent protein has a finite photon budget. A GFP molecule is only capable of sending out some ~10^6 photons, and once that budget is expended, the protein will have irreversibly bleached (Plank et al. 2009; Leake 2013). Thus, hardware requirements are high. A large enough light dose to excite the tags is needed, but at the same time this should preferably be kept as small as possible to postpone the bleaching for as long as possible. With the equipment developed it is possible to use power densities of up to around 2.5-3 kW/cm^2. At these levels only 5-20 frames imaged at 5 ms per frame will be available before any one fluorophore irreversibly bleaches. At the same time on the emission side, full control over the EMCCD is needed to synchronise the two events of excitation and detection.

The developed software automates the process and uses a unified programmatic flow, controlling every aspect of the fluorescent microscopy experiment:

- Laser control – power and emission state

- Camera control – imaging parameters, exposure time, camera gain, Region Of Interest (ROI)
- Sample position – The nano-piezo stage can adjust the sample position within a 300x300x300 μm cube, with nanometre precision through closed loop feedback control.

Thus most operations after initial setup can be performed from within the software suite developed. Some controls, for preliminary focussing, coarse positioning and control of bright-field illumination for reference imaging are not integrated in the software and does require the microscopist to operate these features independently.

2 Imaging Living Cells

One goal of the ISOLATE programme is to develop new techniques to gain insight into the inner workings of living cells. Primarily yeast of the *Saccharomyces cerevisiæ* variety is targeted. The well-characterised fungus has been chosen as a model organism for eukaryotes. The microscope system has been developed with this in mind, but in the project described here, a variant of *Escherichia coli* with the replisome tagged with a yellow fluorescent protein (YPet) was used to show the systems capabilities on live cells.

A living single cell organism such as yeast or *E. coli*, has the same basic requirements as any living organism: consumption of some nutrient and reconfiguring it to a less energy dense metabolite and using the harvested energy to perform actions such as multiplying, going after the next morsel of sustenance or moving away from an unfavourable area. The higher the organism, the more complex the response chain, but for the simplest organisms on this planet, single cell organisms such as bacteria, fungi and algae, the response is quite directly a reaction involving biochemical feedback mechanisms that trigger a response such as e.g. movement away from an area with a too high pH or towards an area with higher glucose content. The feedback is acting through intricate biochemical signalling pathways, which, especially in eukaryotes, can be very long and complex and can also have significant crosstalk between different pathways (Shashkova et al. 2015; Saito 2010; Hartwell et al. 1999; Siso-Nadal et al. 2009). The pathways are made up of cascades of protein-protein interactions from receptors e.g. in the cell membrane, in multiple steps to the nucleus where the signal

triggers transcription of certain genes and consequently production of encoded relevant proteins.

Using of genetically integrated fluorescent protein tags, such as Green Fluorescent Protein (GFP) is a well-established technique used to image features inside cells, in both prokaryotes and eukaryotes. The protein was originally described and extracted from jellyfish called *Aequorea Victoria* in 1962 by Osamu Shimomura, Frank Johnson and Yo Saiga as a down-converting companion protein to the bioluminescent aequorin that itself emits blue light (Shimomura et al. 1962). The down-converting properties make the cnidarian fluoresce in green even if the actively luminescent protein emits blue light. GFP was genetically sequenced in the early 1990s (Prasher et al. 1992) giving rise to a new era in functional microscopy (Tsien 1998; Leake 2013) and has since, together with other derivatives been developed to give fluorescence in a wide spectrum from cyan to far-red wavelengths. Emission wavelengths can be found ranging from 475 nm (Cerulean) to 649 nm (mPlum). A good overview of some available fluorescent proteins (FP) have been compiled by Nathan C Shaner & al. (Shaner et al. 2005).

It is possible to attach fluorescent proteins to functional proteins of interest like a "dongle". Many fluorescent proteins are quite small, being a few nanometres long. Typical length scales are around 2-4 nm (Leake 2013). The structure of GFP is a barrel shape consisting of β−strands surrounding a structure that makes up the fluorophore. The whole structure weighs in at 26.9 kDa (Ormö et al. 1996). The way these structures are attached to the functional proteins under investigation is by splicing the genetic code for the fluorescent protein adjacent to the code for the functional protein. It is also sometimes advisable to include in the code a "tether" of suitable length and configuration. Both the functional and the fluorescent protein will then be produced simultaneously.

Fluorescent proteins are indeed less bright and less efficient than other fluorescent markers such as organic dyes or even quantum dots. The proteins also bleach much faster than other dyes but has the immense advantage of being produced within the cell if the protein code has been genetically integrated. Most other fluorophores need to be internalised, i.e. introduced (by force) into the cell from the outside. This is not an entirely trivial task. An integrated protein is produced within the cell as a normal part of the cells life. It can thus to some extent be dynamically replenished as long as the cell is alive. The fluorescent protein, being a fairly large addendum to a functional protein can possibly interfere with the function of the same. Thus, any results should be reviewed carefully to confirm that the tagged protein is still active.

3 Microscopy

In this project a standard T*i* microscope body from Nikon was used. The configuration is an inverted, combined epi-fluorescence and dia-illumination setup. This gives some advantages; it is possible to locate a sample using low power dia-illumination that is less likely to bleach the sample. Reference bright-field images are acquired in this mode, which can later be superimposed on the images of fluorescence. Excitation light for fluorescence imaging is coupled into the system through a modified attachment for mercury lamps. At the lamp port is placed a module containing a double telescope to expand a laser beam and to steer it into the correct beampath through the microscope.

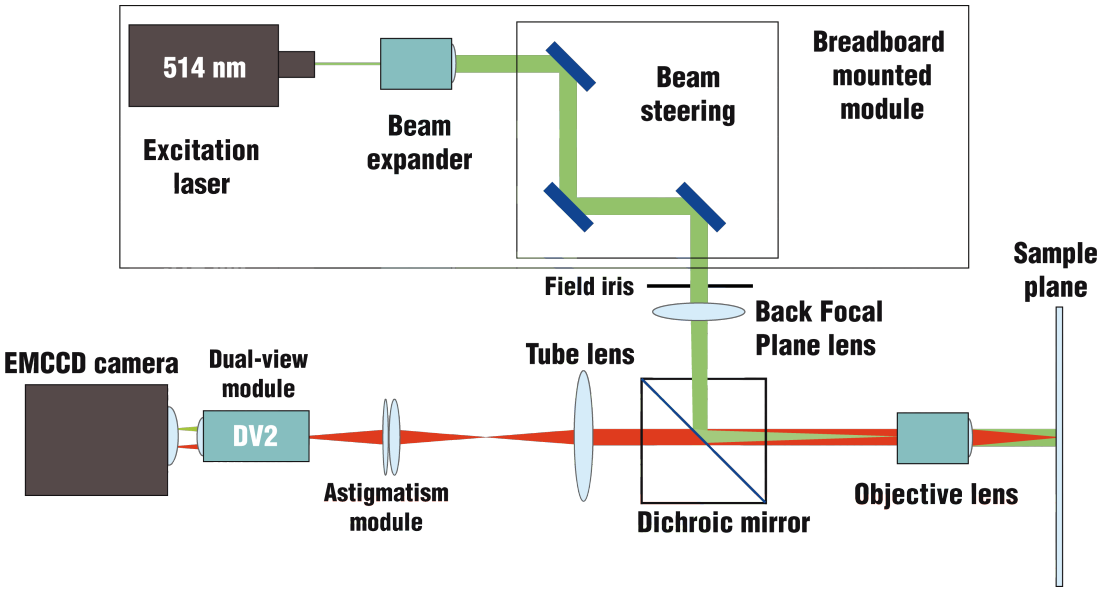

Figure 1 – General schematic of the microscope system

The upper box contains the excitation module, mounted on a 300x400 mm^2 breadboard, the lower half is the imaging path.

An overview of the microscope system is shown in figure 1. See figures 2-4 for more detailed schematic layouts of the excitation module, the microscope beampaths and the imaging beam path and modules. Figure 5 shows a photo of the actual excitation module built.

The beam expander (fig. 2 and 5, lenses L_1–L_2) ratio was chosen to 1.5:4 as this gives an illuminated spot in the image plane that will fill the camera field of view nicely. The camera has a sensor of 512 by 512 pixels. Imaging a graticule with lines etched at 10 μm intervals, it could be determined that 106 pixels corresponds to 10 μm and thus every pixel on the camera corresponds to squares with 94 nm sides at the sample. It could further be concluded that the illuminated field is approximately 48 μm in diameter, being 512 times 94 nm.

After the beam expander, two mirrors, the second of which is placed in the focal plane of lens L_3, perform the beam steering. Lens L_3–L_4 is a 1:1 telescope effectively translating the resulting beam angles from the second mirror to a position 2 focal lengths ($2 \cdot 134.8$ mm $= 2 \cdot f_{BFP}$) from the back focal plane (BFP) lens. The BFP lens in turn focuses on the back focal plane of the objective lens. This arrangement allows proper beam steering using the two mirrors between L_2 and L_3.

A diode pumped 514 nm solid-state laser of the brand Obis was used to provide excitation light for the experiment involving organisms containing YPet. The wavelength 514 nm, was chosen for being well suited for exciting several varieties of Yellow Fluorescent Proteins – YFP or YPet (Shaner et al. 2005). The available power density at the sample is up to around 2.5-3 kW/cm^2; with a nominal laser optical power output of 50 mW. Measuring transmitted power at the sample and correlating this with the illuminated area confirmed this value.

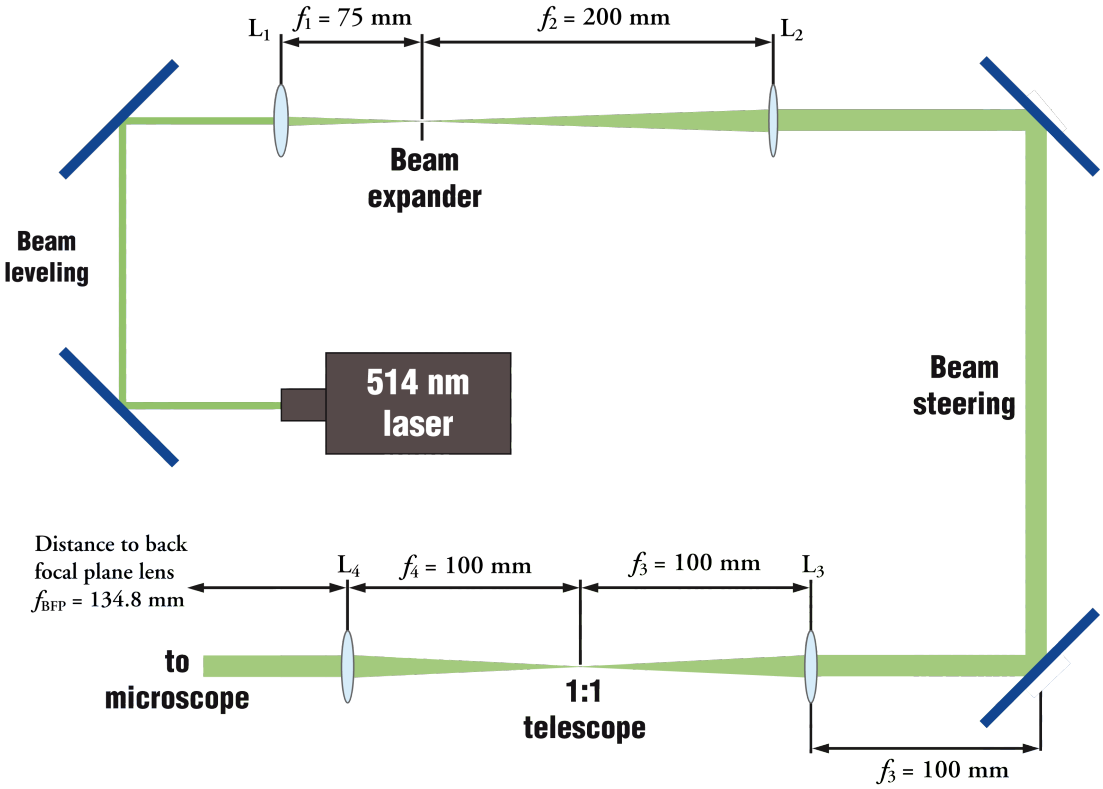

Figure 2 – Schematic of the excitation module. Including two Keplerian telescopes, one beam expander and a 1:1 telescope for beam transport. See also figure 5.

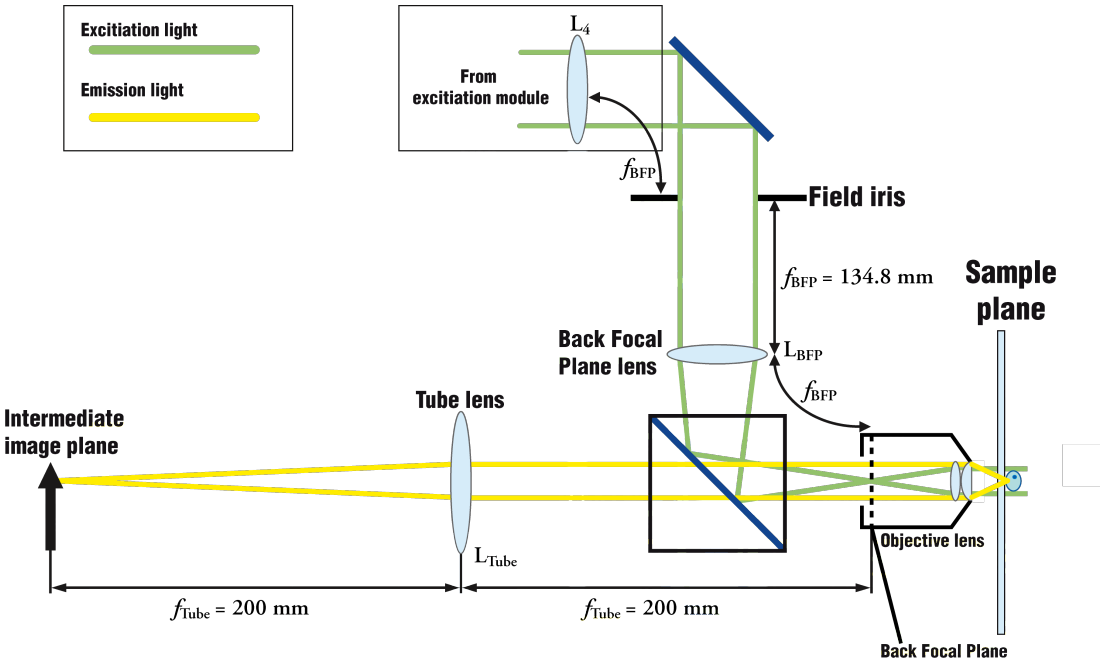

Figure 3 – Schematic of the microscope excitation and imaging paths. The image at the intermediate image plane can be either projected directly onto an image sensor or imaged by further optics as is the case in the microscope described here.

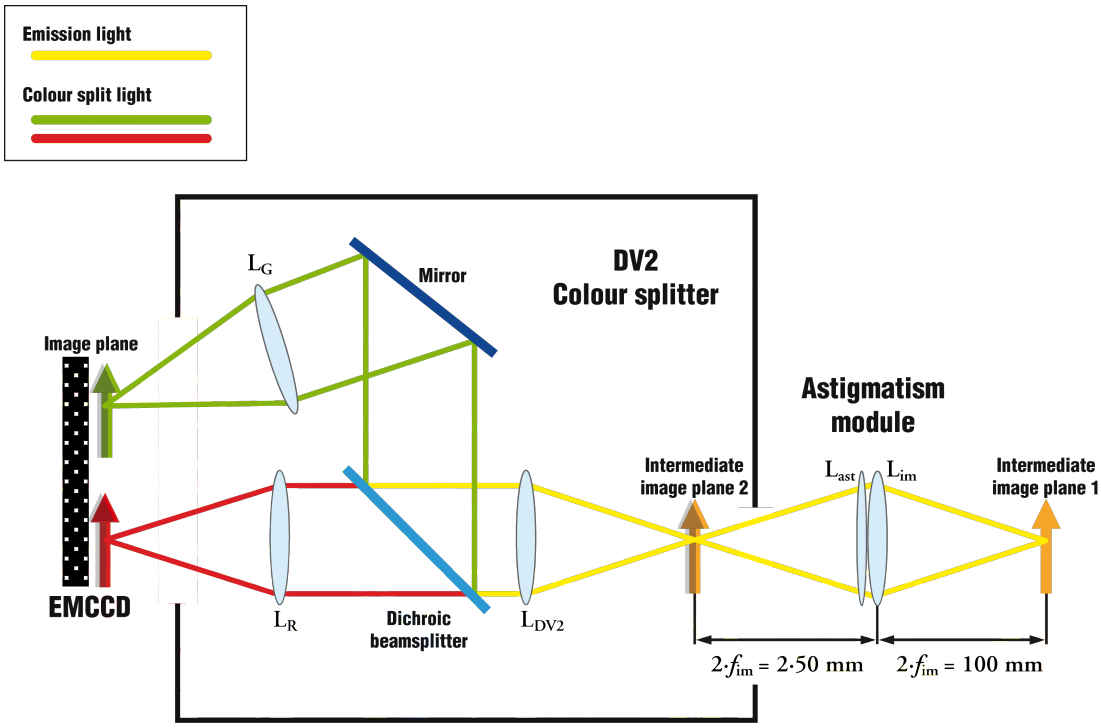

Figure 4 – Following from the intermediate image plane in figure 3, here the final imaging path is shown. The elements in the box, "DV2 Colour splitter" are part of the commercial DV2 dual-view package.

The part contained within the Nikon T*i* body is shown in figure 3. Excitation light is shown as green beams and emission light as yellow beams. The intermediate image plane is the image plane shown in figure 4 as *intermediate image plane 1*. The final imaging path, shown in figure 4, starts at this plane and passes through the *Astigmatism module* which consists of an imaging lens of 50 mm focal length and the spherical lens of 1000 mm focal length along one axis that can be inserted as necessary when astigmatic imaging is required. The 4*f* configuration between the two intermediate image planes ensures that a 1:1 image is projected into the DV2 Colour splitter and subsequently onto the final image plane at the EMCCD camera sensor.

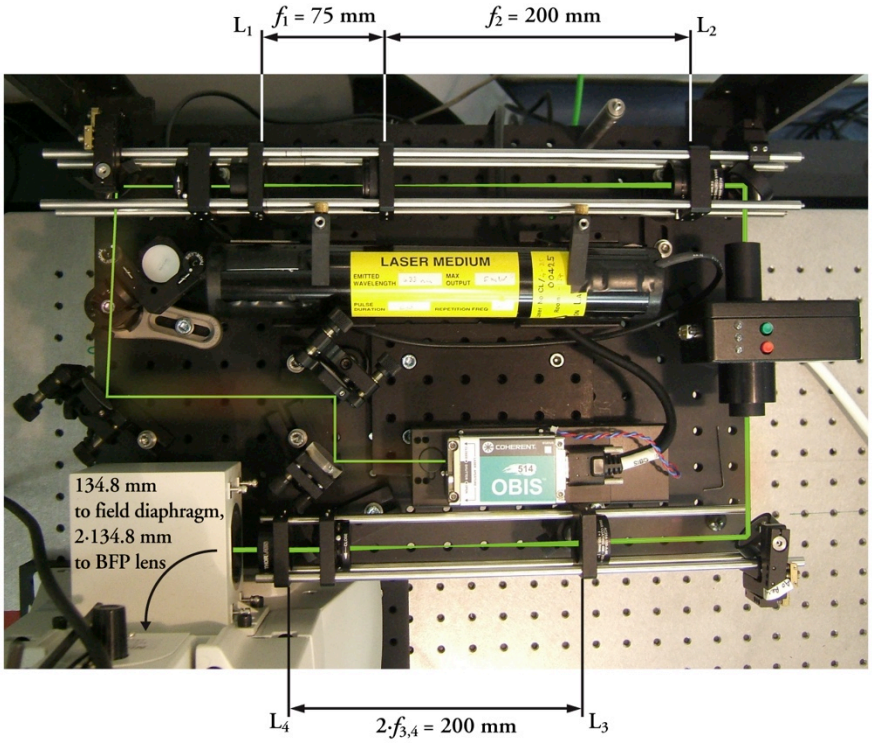

Figure 5 – Actual layout of the excitation module configured for use with 514 nm excitation light, suitable for YFP and YPet excitation.

The fluorescent proteins are, as earlier mentioned somewhere between 2 and 4 nm big. This is far below the Abbe limit and thus the fluorophores can be considered point sources. When imaging a point source through a microscope the resulting image will be an Airy Disk. The Airy Disk is a function of the optics involved in the imaging system. Viewing point sources in a specified plane with the optics adjusted to image that plane, initially the effects of out-of-plane imaging can be disregarded. The following can be said of the resolution and the size of the images projected onto the detector.

The *Numerical Aperture* is defined as:

$$\mathrm{NA} = n \sin \vartheta \qquad (1)$$

Where *n* is the refractive index of the imaging space, i.e. the medium between the sample and the objective lens. See figure 6 for clarification.

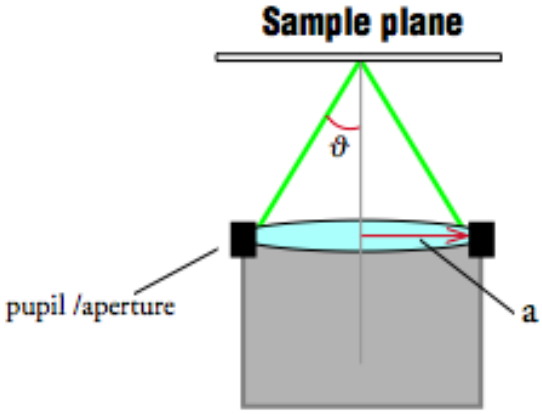

Figure 6 – Numerical aperture of a microscope objective lens
Image from Erik Hedlund - *Construction of a Scanning Laser Confocal Fluorescence Microscope System for Single Molecule Detection and Spectroscopy* (Hedlund 2011)

This quantity is intimately interconnected with the minimal size of the image ultimately projected onto the detector. In this case an EMCCD camera is used. The Airy disk can be described by the following equation for in-plane sources. This nomenclature was also used by Webb (Webb 1996) in his description of the provisions for confocal microscopy which are applicable in this case as well. In equation (2) a quantity, ρ, often called an *"Optical Unit"* (o.u.) is defined for the transverse (in-plane) dimensions. It is well worth noting that in some literature this quantity goes by the alternative designation *v,* used by e.g. Born and Wolf (Webb 1996).

$$\rho = \frac{2\pi}{\lambda} r\mathrm{NA} = 2\pi \frac{n}{\lambda} r \sin\vartheta = r\boldsymbol{k}' \sin\vartheta \tag{2}$$

Where $\boldsymbol{k'}=2\pi n/\lambda$

The optical unit is a scaled dimensionless variable describing the radius of the rotationally symmetric image of the point source. It is worth noting that this is the case in a normal (ideal) microscopy system without intentional (or unintentional) astigmatisms, something that will be introduced later. The image projected on the camera is an image of the point spread function (PSF):

$$I(\rho) = \left(\frac{2J_1(\rho)}{\rho} \right)^2 \tag{3}$$

Where J_1 is a first order Bessel function, i.e.:

$$J_1(\rho) = \frac{1}{2\pi} \int_{\tau=0}^{\pi} e^{-j(\tau - \rho\sin\tau)} d\tau \tag{4}$$

Thus the rotationally symmetrical interference pattern of the PSF is explained. Now there is also the axial dimension, the Z-axis. The optical unit for this axis can be described similarly:

$$\zeta(r) = \frac{2\pi}{n\lambda} \mathrm{NA}^2 z = 2\pi \frac{n}{\lambda} z \sin^2\vartheta = z\boldsymbol{k}' \sin^2\vartheta \tag{5}$$

The full definition of the PSF is a function of both ρ and ζ.

The central peak in this image will contain most of the light of the image and normally two adjacent peaks are considered resolved if the peaks are no closer than its neighbour's first dark fringe, a distance Δr.

$$\Delta r \approx \frac{0.61 \cdot \lambda}{\mathrm{NA}} \tag{6}$$

This is the Rayleigh criterion. This determines the resolving power for normal microscopy (Wegerhoff et al. 2007; Leake 2013). As an example for YPet, emission at 530 nm would, using an NA=1.4 oil immersion objective lens, give a minimal distance between resolved spots of 0.23 μm.

4 Super-resolution Techniques

Several established super-resolution techniques were considered to pinpoint fluorophores within living cells. In the introduction were introduced two methods, the astigmatism approach and the DH-PSF.

A wide-field microscope that is imaging close to the diffraction limit can be modified on the imaging side to provide more information in the Z-direction than what seem to be available at a first glance. The resolution in the axial dimension in an un-modified system is quite low due to the size of the depth of field, which is a few hundred nanometres in the case of a 100x oil immersion objective lens with a NA of 1.4. This is to be compared to the precision of a few 10's of nm in the lateral plane.

The change of size of the image is quite small for the standard imaging system. In figures 9 to 14 a sequence of images of 100 nm fluorescent beads taken at the focal plane, at ±50 nm and ±500 nm are shown.

Since the fluorophores that are investigated are much smaller than the wavelength of the emitted light (a fifth in the case of the beads, a 100th to 200th of the wavelength in the case of proteins) the beads and proteins imaged can be considered point sources. If the fluorophores are sparsely distributed, in such a way that pairs or larger clusters of fluorophores seldom are co-located, it is possible to determine the in-plane location of one fluorophore with much higher accuracy than would have been possible in a cluttered image with several unresolved point sources (Betzig et al. 2006; Hess et al. 2006; Rust et al. 2006). The centre peak of the PSF is quite similar to a Gaussian and a well established method of finding locations of diffraction limited point sources is to fit Gaussians to the imaged Airy disks central peaks and finding the centroids of these. The result is also ultimately limited by the pixel density of the camera as the spatial

resolution in the imaging plane how finely grained the quantisation of the incoming image will be.

When the purpose of the imaging is to precisely locate a point source in three dimensions and no major consideration in taken to more complex patterns, it can be worthwhile to consider using a PSF shaping technique that enhances the axial resolution. The purpose of this microscope is to be able to pinpoint the locations of single fluorescent proteins. These are ideally spaced with low enough concentration within a cell for microscopy to be straightforward. This may or may not be true directly depending on the abundance of the tracked protein, but the photophysics of high intensity excitation light will over time bleach the number of fluorophores to a point where this is true.

The main goal has been to improve the axial resolution (z-direction) to if possible match the in-plane resolution (x/y-directions) and the choice ended up falling on the astigmatism approach, as it is simple to implement and robust, even though the precision gain may be slightly worse than the DH-PSF. The DH-PSF method has a few traits working against it, compared to the other methods discussed here. It requires an extremely well aligned phase mask, which cannot easily be removed from the beam path when imaging bright-field or DIC images of cells. This could introduce an obstacle if a fixed phase plate is used, as images are distorted by the mask. The problem is less of an issue if an SLM is used, as this can be set to a uniform phase delay, but such a device introduces a hit on the transmitted/reflected light, some 10% may be lost in this component.

On the emission side, a commercial dual-view colour splitter optics package from *Photometrics* (manufacturer of cameras and optical solutions) allows for simultaneous dual colour analysis. Something that becomes important when following interactions

between proteins tagged with different fluorescent markers in living cells. This feature was not used in the work described here. The dual-view package has a pass-through mode, which was used for the duration of the measurements described here. The splitter package also works as a 1:1 telescope so that an image projected on it will be projected without further magnification on the image sensor, which is located at the conjugate plane of the telescope imaging lenses.

The simple yet powerful technique to introduce an asymmetry in the imaging pathway, is accomplished by placing a cylindrical lens (focal length 1000 mm) component in tandem with the final imaging lens (see figures 4 and 7) that projects the image on the EMCCD via the colour splitter (remember that the dual-view filter that separates the image in two wavelength bands also acts as a 1:1 telescope so one intermediate image plane will be in the dual-view tube). The final imaging lens (L_{im}) is a single 50 mm achromatic doublet mounted in a 4f relation to the intermediate image plane (located just outside the microscope side port, see the physical layout in figure 8).

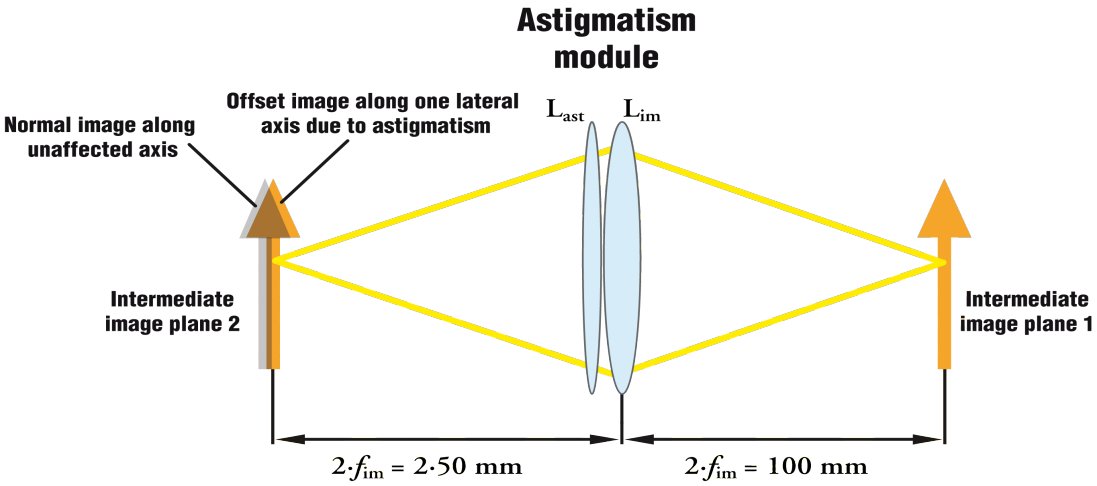

Figure 7 – Detail of the beampath in the astigmatism module

The astigmatism deforms the image projected on the camera in a very specific way: If a point source is located in the systems focal plane the image will be fairly similar to that of a non-astigmatic system, but with the source moving out of the focal plane a distinct deformation of the image will occur. The effect is that the symmetric image of a point source in the focal plane elongates in either the X or Y direction depending on whether the fluorophore is moving closer to or further away from the objective lens. This method was implemented in this microscope and the effect is quite pronounced and can even be noticed by eye in figure 12. The same sample has been imaged without astigmatism in figure 9 and with the astigmatism module in figure 10. The sample is imaged again with and without the astigmatism module installed, axially shifted 50 nm in figures 11 and 12 and axially shifted 500 nm in figures 13 and 14. By measuring this asymmetry a more accurate value on the proteins displacement can be calculated than would be possible using standard imaging. At the same time the centroid does not move due to the introduced astigmatism so when finding the position in the transversal planes, the astigmatism technique still give the same result.

The precision of the localisation of an imaged spot is determined by several factors (Thompson et al. 2002). The background noise, the shot noise, the number of photons collected, the size of the spot image and its relation to the camera pixel size. Thompson arrives at some important conclusions relevant to imaging single proteins: an estimate for the lateral precision of the localisation and an optimal size of the image on the detector. In a situation where the measurement is dominated by photon noise the localisation precision is given by the standard error on the mean:

$$\langle (\Delta x)^2 \rangle = \frac{s^2}{N} \tag{7}$$

Where s is the standard deviation of the PSF size and N is the number of collected photons. In addition to this general precision, the actual precision is further determined by the additional factors: Background noise – photons coming from other sources than the particle of interest, e.g. autofluorescence and readout noise. The pixel size – affecting the spatial quantisation of incoming light. Taking all these factors into account, the real combined two-dimensional localisation precision is described by the equation:

$$\langle(\Delta x)^2\rangle = \frac{s^2+a^2/12}{N} + \frac{8\pi s^4 b^2}{a^2 N^2} \quad (8)$$

Where b is the background noise and a is the pixel size. As before, s is the standard deviation of the spot size and N the number of photons.

Thompsons estimate of optimal pixel size to be about the size of the standard deviation of the PSF also stems from these calculations and shows that for a fixed number of detected photons and constant background noise but varying the pixel size, the smallest localisation error is obtained when the pixel size is around the same size as the standard deviation of the PSF. The microscope system is very close to this optimum when imaging fluorophores without astigmatism as can be seen in figure 9. However, due to the nature of the astigmatism technique, this does not hold true for images in this mode. In figure 10 can be seen how the imaged spots are larger in the lateral dimensions. Consequently the lateral precision will be somewhat worse than in a non-astigmatic system.

In the case of a cell having a high concentration of fluorophores the camera may saturate. A solution to this is to pre-bleach a specific area by shining a high power laser on the area of interest for a short moment prior to the actual investigation. The bleached area will have fewer or even no emitting bodies, but as unbleached proteins from outside this region diffuse into it singular responses can be collected.

The dual-view filter, splitting the emission light in two wavelength bands is fitted as this allows for simultaneous tracking of two distinct populations of proteins. This setup also allows future use of *Förster Resonance Energy Transfer* (FRET) to track interactions between two tagged proteins.



Figure 8 – Actual layout of the imaging path of the microscope. From right to left: Camera, colour splitter (in by-pass mode), cylindrical lens and 50 mm imaging lens
The first intermediate image plane is just beyond the end of the metal rods protruding from the colour splitter. See also the schematic in figure 4.

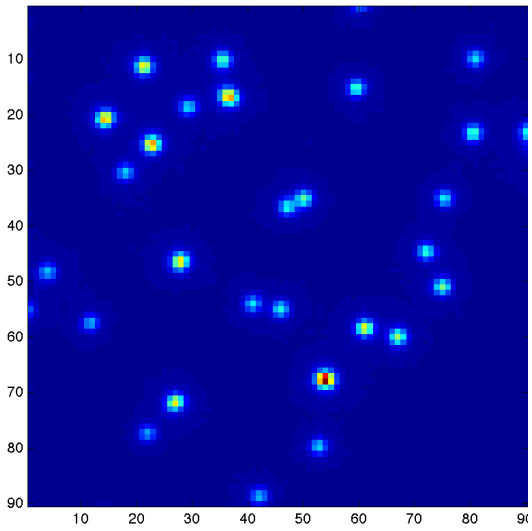

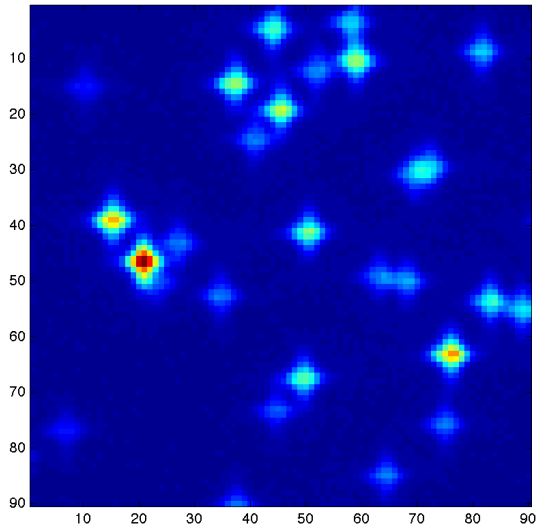

Figures 9 to 14 – Images of fluorescent beads at the focal plane of the microscope. The image on the left hand side is without the astigmatism module and the image on the right hand side with it.

Below -50 nm (top row) and -500 nm (bottom row) right and left as above

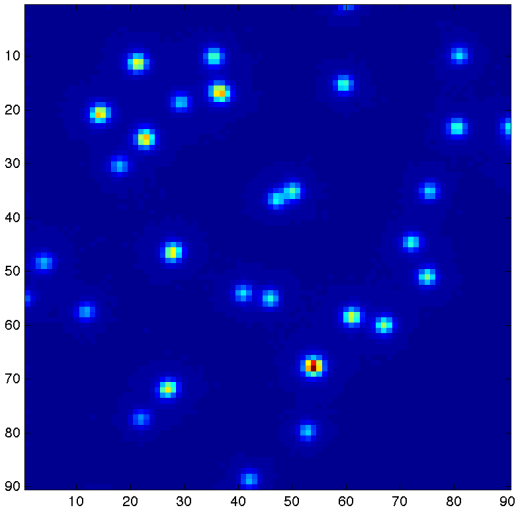

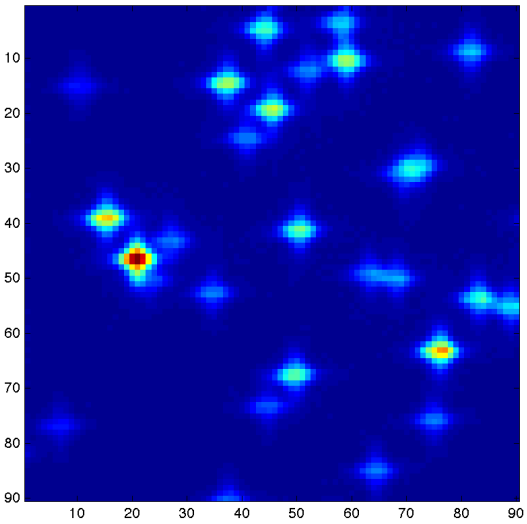

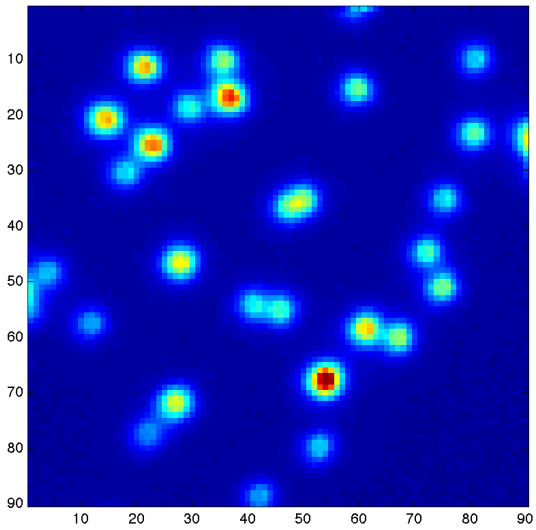

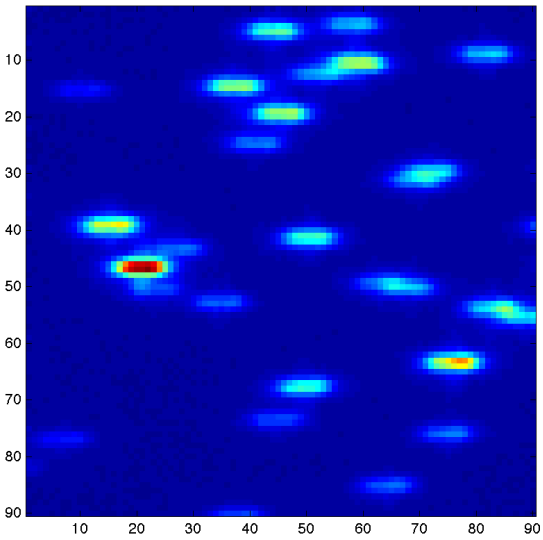

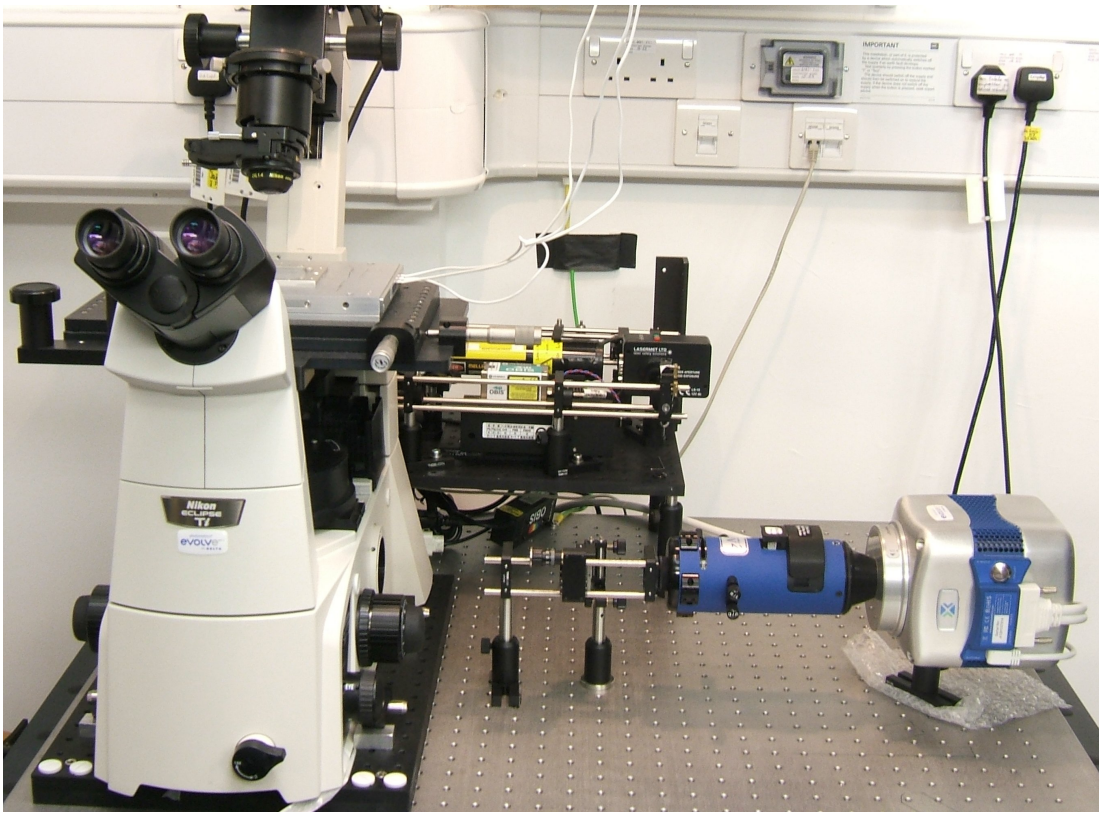

Figure 15 – System overview

Left, Nikon T*i* microscope. Middle rear - excitation module. Middle front and right, astigmatism, colour splitter and EMCCD camera.

5 Characterisation

To characterise the system, 0.1 μm fluorescent beads was used. Beads this size are smaller than the wavelength of the fluorescence light and can be considered point sources for characterisation purposes.

5.1 Preparation of flow channels for beads

To prepare a sample that can be used for characterisation of the system a sample with a single layer of sparsely located beads is ideal. To get as close to this ideal as possible a preparation was made from a stock of orange (excitation peak 540 nm, emission peak 560 nm) *FluoSpheres* carboxylate modified fluorescent beads. The stock contains 2% solids and was diluted 2000 times before being applied to a coverslip. The application was done by creating a very simple flow channel created of a sample glass on which two strips of double-sided tape was attached. The coverslip was then attached as a bridge between the two pads of tape. This arrangement leaves a thin channel, a millimetre or two wide, between the two tape strips and the glasses, see figure 16. This channel can be filled with capillary forces from a pipette and a piece of tissue paper on the opposite side used as a wick to create sufficient flow. After flowing the suspension through the channel the prepared sample was left to rest for a while with the coverslip downwards so that gravity would let the beads to settle on the coverslip, 15-30 min would normally be enough. Too many beads suspended in the liquid in the channel makes it hard to find a well-defined plane to focus on so ideally all beads should be deposited onto the coverslip. As this is not attainable the method used is to focus on the first plane with a set of deposited beads, not taking into account the out of plane beads.

After this preparation the sample could be used and reused multiple times as the beads tend to stick to the glass surface, are quite stable and does not photobleach very quickly. It will be necessary to re-wet the sample from time to time, as the water will evaporate over time.

5.2 Data from living cells

A test on biological matter could be carried out using YPet-tagged *Escherichia coli* of the same type used by Reyes-Lamothe to find that the large replisome complex that copies DNA in *E. coli* comes in triplicate on each replication fork (Reyes-Lamothe et al. 2010). The mutant has a YPet tag attached to the replisome component ε, that is a part of the Pol III complex. The ε-YPet thus also comes in triplicate. In total, each cell holds six YPet molecules (three molecules per fork), usually distributed to two foci with three molecules each, but occasionally it is possible to find cells where all six are colocalised in the centre of the cell.

During the live cell experiments the same protocol for cell cultivation was used as Reyes-Lamothe and Oliver Harriman described (Harriman 2013; Reyes-Lamothe et al. 2010). Cells were grown in LB overnight and then sub-cultured in LB for an additional 3 to 4 hours to an OD_{600nm} of around 0.02. The culture was centrifuged for 2 minutes at 5500g and the supernatant was removed and the cells resuspended in PBS. To prepare a sample for microscopy the same type of flow channels described for beads was used. The channel was first treated with 0.1% polylysine and incubated for a few minutes, after which the remaining polylysine was washed away with 100 µl PBS. The cells suspended in PBS were then introduced. After 15 minutes incubation time, the sample was once again washed with PBS to remove unbound cells and the sample was ready

for microscopy. A sample like this will have a density of cells comparable to the bead sample shown in figure 20.

The camera was run with an electronic gain of 300x and images were captured with 5-40 ms exposure times. Data was saved in TIFF files and kept for later offline analysis.

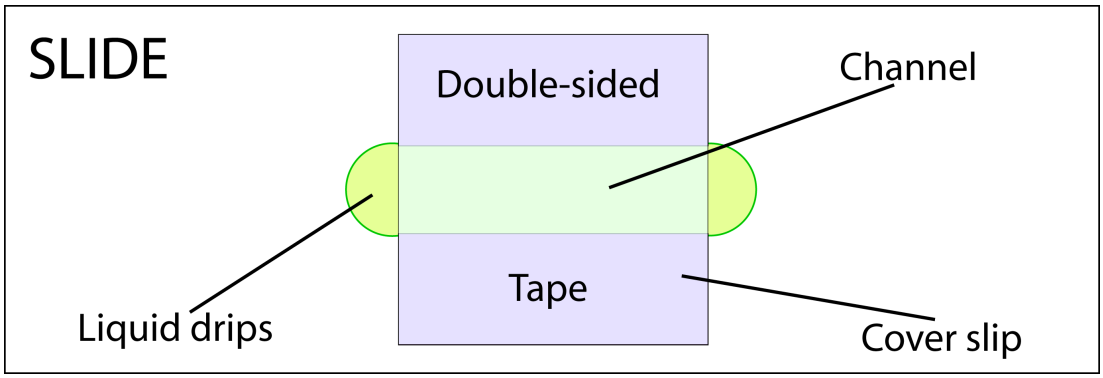

Figure 16 – A simple flow channel created by sticking a cover slip as a bridge between two strips of double-sided tape. The channel width is 2-4 mm. The liquid drips on either side of the openings delays the drying out of the channel.

6 Software design

Design concepts of the control software, including ideas of remote control will be covered in this chapter.

The microscope system is controlled via a unified user interface developed in LabView. Main characteristics on the main user interface are a large display, showing the image from the camera, and a tabbed control pane. See figure 17. In appendix A selected key sections of the LabView acquisition software source code are included. This simple yet effective GUI design was chosen to ensure an operator should not need an in-depth knowledge of the inner workings of the software to be able to use the microscope.

Functionalities are grouped together in as intuitive a way as possible. Camera related settings have been placed in an **'Exposure and Initials'** section encompassing exposure, camera temperature, EM gain settings, Initial Region of Interest (ROI) and command rate. The current design does not allow for change of most of these settings (except the ROI) while the main controller is running. One reason for this is the way initial values are set on the camera. Resetting of the camera before entering new values make sure the new values do not compromise the state the camera is in. To set new initials the camera control system must first be halted by pressing the 'Stop' button in the 'File' tab. This gracefully releases all handles and brings the software back to the initiation state. The software remembers the last selected ROI and uses this as the initial ROI the next time the controller is started again (if LabView itself is stopped, for any reason it does however *not* remember the previous ROI state unless the user specifically saves this state.

While running, the two tabs **'Acquisition'** and **'Programme'** contain controls to manipulate the sample and illumination. On the acquisition pane (see figure 18) are controls to move the sample in three dimensions using the MCL nano-piezo stage.

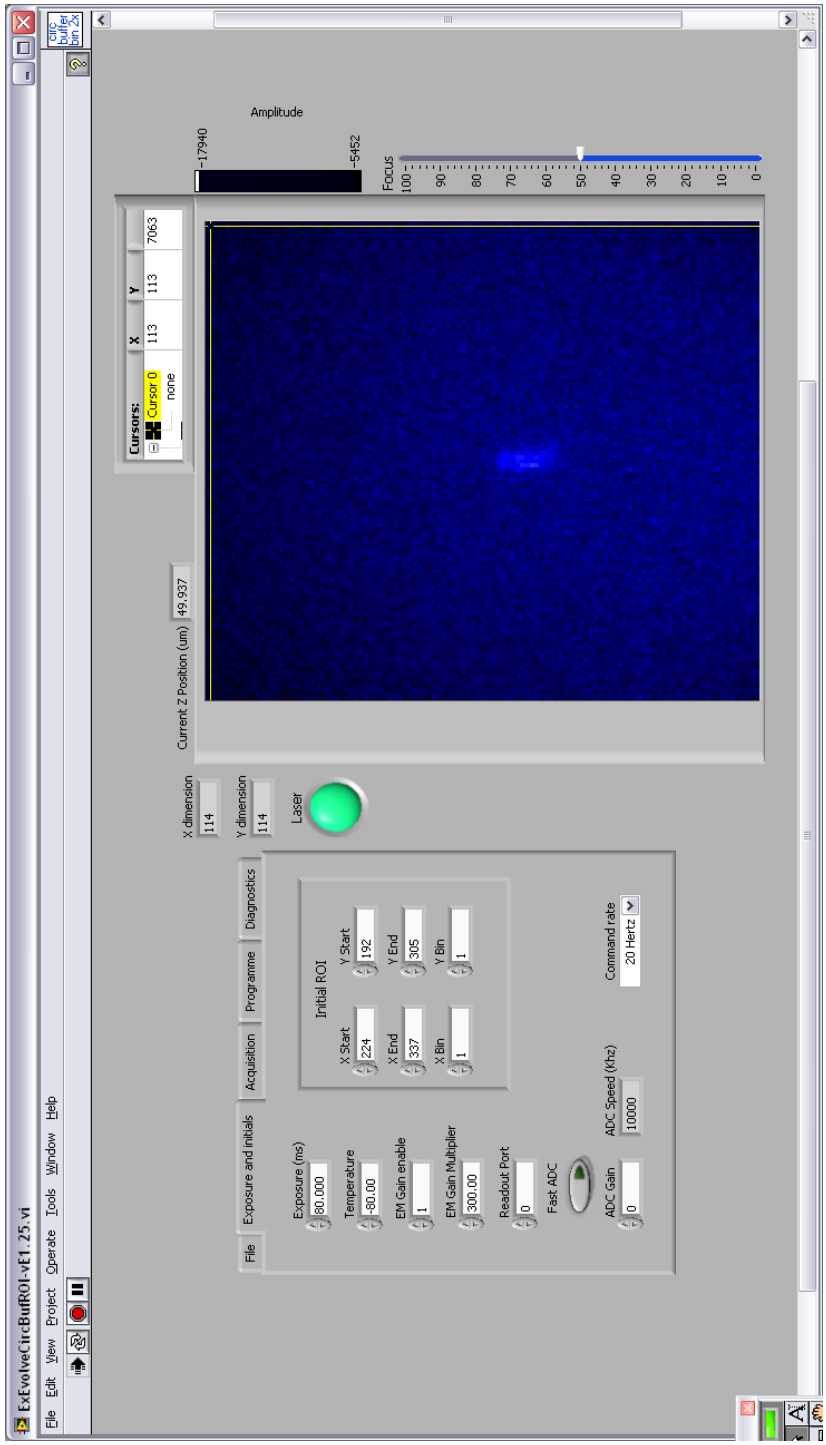

Figure 17 – Camera control and imaging software front panel

Four buttons are available to shift the sample in the *x-y* plane and a slider to control the axial (focus) dimension, for refocusing etc. A toggle switch for the excitation illumination is also available. This is for localisation of cells in the sample.

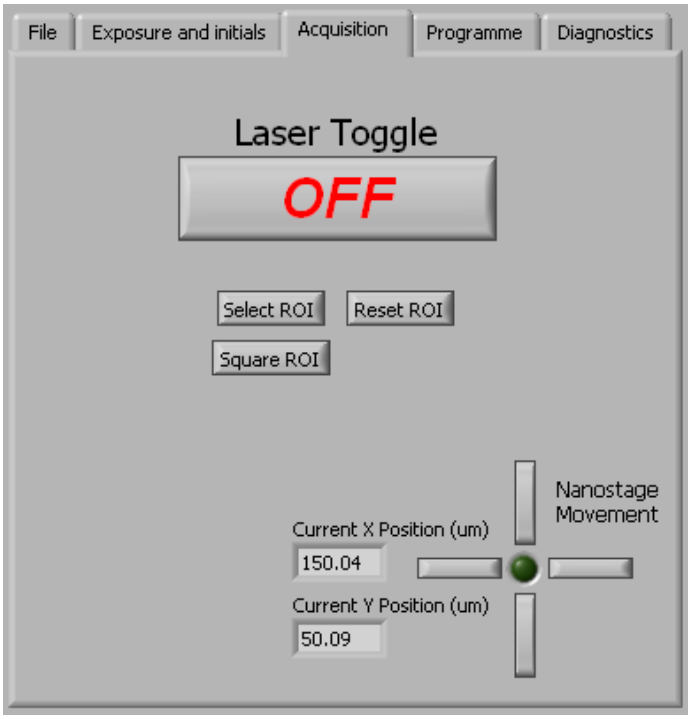

Figure 18 – Acquisition control, setting of ROI and fine-tuning of position. The laser on-state can be manually controlled from this pane

On the programme pane (figure 19), sequences of image acquisitions can be programmed and executed. The sequences can involve shifting of the sample along the z-axis i.e. moving the focal plane through the sample, for every frame (z-stacks). This data can from here, if the user so wishes, be saved to tiff-files and/or text files (some source code alteration is needed if the user wishes to turn off saving of either file type). Pressing the "run" button will execute the programme – Move to the end point of the z-levels, turning on the laser, acquire one frame, move the stage, acquire next frame and so on until turning of the laser after the final acquisition and returning to the idle state.

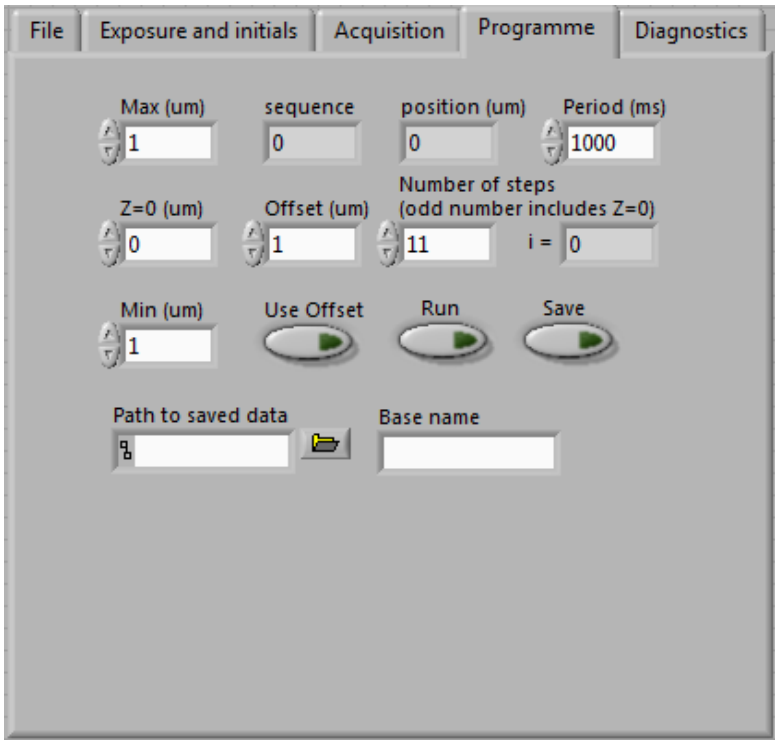

Figure 19 – Sequence programme control pane

The programme is mostly nested in subroutines in the way National Instruments suggest as good coding practice. Parts of the code are loosely based on demonstration snippets from the providers of drivers for the nano-piezo stage (Mad City Labs) and the EMCCD camera (R-cubed for Photometrics). See appendix A for images of the source code for core functionality.

Experiments of the type this system is designed for are in general very sensitive to stray light and the signal to noise ratio can be quite bad. Thus there can be an incentive to provide for an opportunity to control an experiment from another locale than the actual lab space where the setup is located. This allows bright devices such as lights and screens to be turned off in the lab space and full control over the experiment can be had from e.g. an adjoining room, or even in an office somewhere else. A simple

solution for this was implemented using a VNC connection with the controlling machine.

6.1 Considerations

Modern LabView versions are multithreaded environments; in which fully parallelised implementations of complex software can be built. This is needed as data collection and control will be performed simultaneously.

Imaging with short exposure times at high speeds generates large data flows. At frame sizes of 512 by 512 pixels and a bit depth of 16 bits per pixel, every frame generates half a megabyte of data. With 5 ms exposure times, shot back to back this would mean 200 frames per second would generate 100 MB per second. However, there are some limits to the frame rate the camera system used can achieve due to the physical properties of the imaging chip and control hardware. The camera cannot image at a frame rate of 200 frames per second at full chip, 512 by 512 pixels, frames, but this is not a problem in this project. Images are acquired at 5 ms exposure time, which is the time critical point to show the feasibility of short exposure time positioning. But the frame rate is not critical as the stage is shifted between acquisitions and a short delay is needed between frames to allow the stage to settle. Shorter sequences are buffered in the camera and shifted over the FireWire high-speed interface to the acquisition control computer.

7 Data Analysis

Data from bead samples were collected in three main categories:

- Long series, 100-200 shots or time-logarithmic series of up to 32 minutes to determine if the piezo-stage or any other component has a systematic drift
- Astigmatic series, taken at positions with sufficient bead density
- Non-astigmatic series, taken of the same samples, without moving the sample as a reference

The number of counts registered on the EMCCD sensor would be found in the range between a few hundred counts per second – the dark count level and several thousand counts imaging a bright bead. Care was taken to avoid saturating the EMCCD at 65536 counts.

A big challenge is to extract information about where on the z-axis a fluorophore is located. Using the astigmatic approach this is done by measuring the deformation of the image that is the result of the added asymmetry in the system (Huang et al. 2008).

Measuring the position of a fluorophore accurately is done by first finding the rough positions where there is an intensity peak and then using the fact that the intensity profile of the central peak of an image of a point spread function can be approximated by a two-dimensional Gaussian:

$$f(x,y) = \frac{1}{2\pi\sigma_x\sigma_y} e^{-\left[\frac{(x-\mu_x)^2}{2\sigma_x^2}+\frac{(y-\mu_y)^2}{2\sigma_y^2}\right]} \tag{9}$$

Where the width in *x* and *y* directions are denoted σ_x and σ_y respectively. This is still true when the astigmatism is introduced but instead of assuming rotational symmetry both dimensions need to be addressed. The asymmetry causes the PSF image to elongate in either the x or y-direction, depending on if the fluorophore is closer to

the camera or further away from it relative to the focal plane. The ratio of the lengths of the fitted axes, σ_x and σ_y will describe how far out of the focal plane a point source is located.

The methodology used here is not a real time approach. Software was developed that was based on a MATLAB software suite developed by Isabel Llorente-Garcia (Llorente-Garcia et al. 2014). The suite finds bright spots in an image sequence by a multistep procedure. Initial threshholding finds candidate spots in an image frame and provides a list of coordinates. The code was modified, adding secondary methods performing 2D fitting to detected spots, to use these initial coordinates to create 31 by 31 pixel subframes. The 2D fitting provides pairs of values for every spot, along the x- and y-axes. The values are the subpixel position and the width of the fit. These pairs of values can subsequently be analysed by using the fact that the size of a PSF will follow a *defocussing curve* that can be fitted to a second-degree polynomial (Huang et al. 2008). The benefit here is that the two axes will follow two slightly offset curves that intersect at the point where the image is symmetric, when the σ_x/σ_y ratio is 1. This means that the minima of calibration curves fitted to either axis do not overlap and the low gradients around these can be avoided by using the sections on either side of the intersection, thus increasing the axial accuracy.

Collected data is kept in tiff-files, which are read by the software suite when analysis is being performed. The software finds candidate spots in the images and selects reasonable candidates to be further investigated. In figure 20 the mid point of such a set created from imaging a bead sample is shown. The set is a 21 frame series with the 11th frame supposed to be placed at the focal plane and 10 frames on either side, each spaced 100 nm from the next in the series. I.e. the range is from -1 μm to +1 μm. From the image a set of spots to be used are chosen.

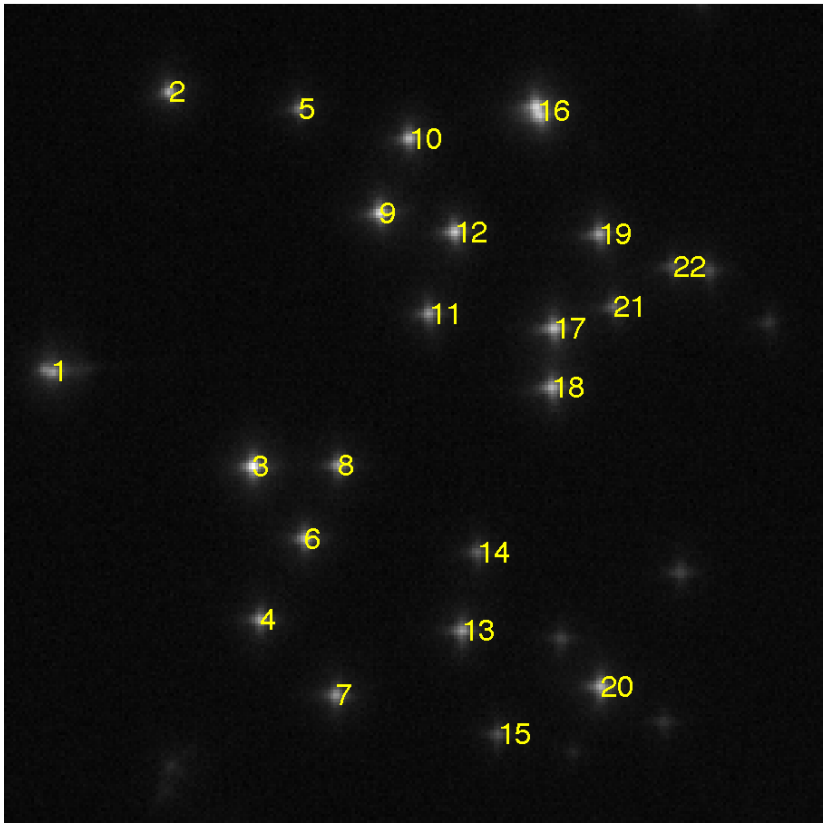

Figure 20 – Automatically selected spots in an image field

Several of the spots in an image can be less well suited for further analysis. Using the example in figure 20 it is easy to see that e.g. spot 1 is very close to the border, which can give problems when using fitting software. Further it can be seen that spot 1 is malformed, possibly due to a second bead being stuck slightly behind the bead. In the detected spots number 16 and 22, both have double beads in the spot and cannot be used. If the fluorophores are located too close to each other they will appear as one deformed spot, and this may affect the method using PSF deformation to determine z-location.

Figures 21 to 25 show spot number 11 from figure 20 at different distances from the focal plane. In figure 21 the focal plane image is shown. The focal plane should be located at the mid-level position, but as coarse focusing is done by eye, in reality it is hard to perfectly place the focal plane. In figure 18 the spot from the 13th frame in the series is shown. This level, corresponding to +200 nm from the mid-sequence frame, is the closest to the actual focal plane. The 13th frame has the values of σ_x/σ_y closest to 1, i.e. a symmetric 2D Gaussian.

Note how the two figures 22 and 23 are symmetrically arranged ±200 nm around the symmetry plane at level 13.

In figures 24 and 25 are shown the frames spaced at ±600 nm (frames 6 and 20). These two are at the limits of what can be reliably detected in a 31x31 pixel subframe. In total this corresponds to a total range of around 1.2 μm.

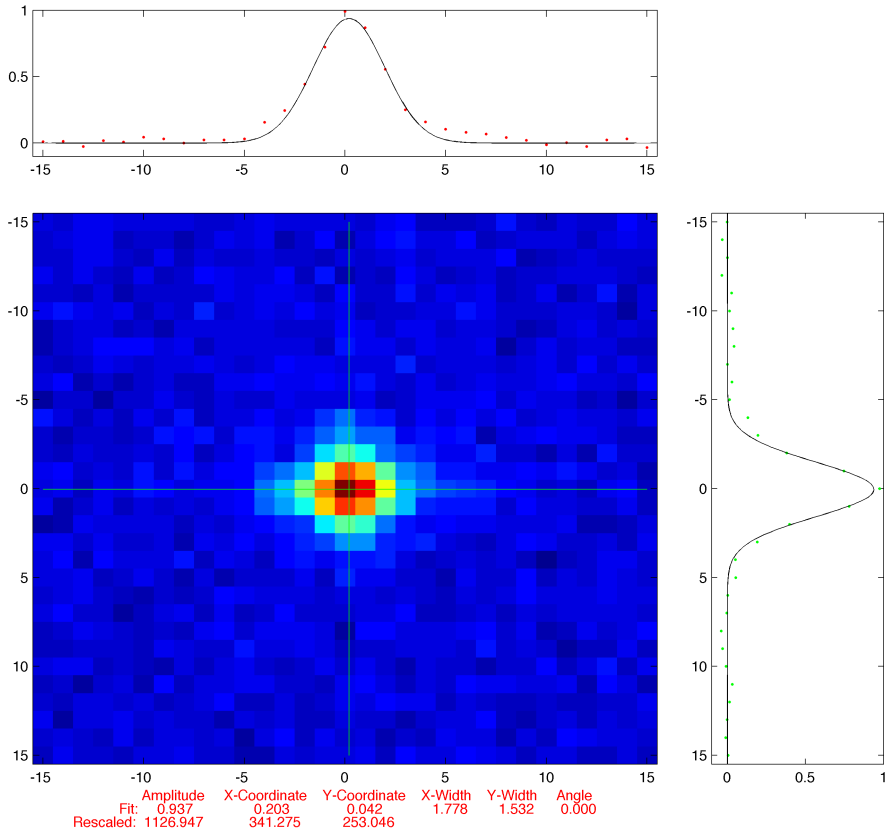

Figure 21 – Spot no 11, bead located at focal plane

The ratio σ_x/σ_y close to 1

In figure 21 is shown a point source (bead) located near the symmetry point. This level is where the two calibration curves intersect.

Again, it should be noted that the way this method works, along one axis the focal plane at the sample is shifted a few nanometres with respect to the unmodified image. This means that at the symmetry point, in reality the image is indeed minutely defocussed along both axes, but the symmetry point can be considered a new, virtual focal plane. This means that the size of a spot image at the symmetry point will be larger than an unmodified image of the focal plane, but the benefits from the deformation balances this, c.f. figures 9-14.

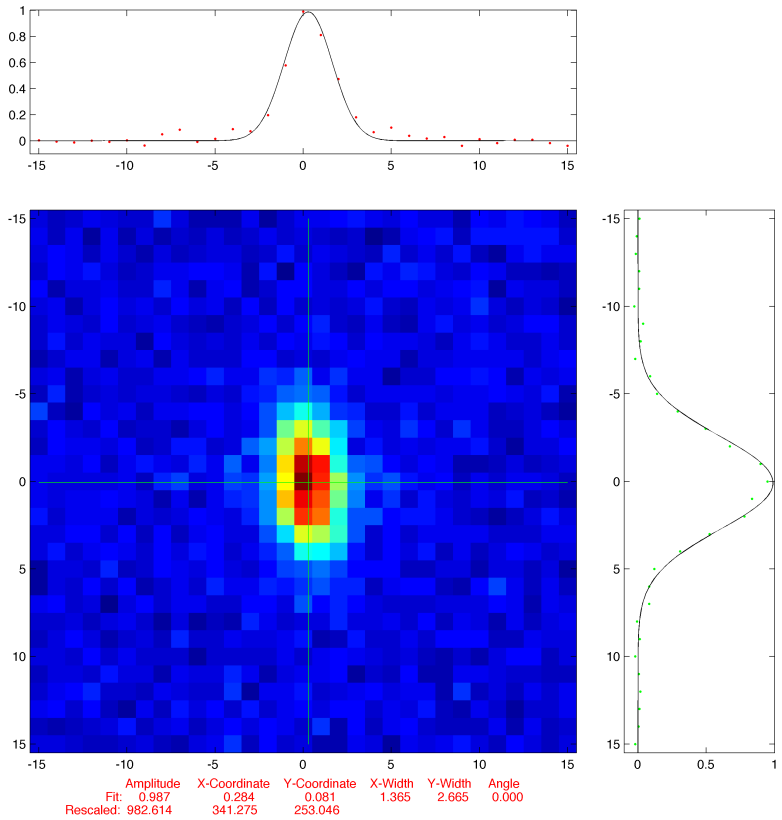

Figures 22 (top) and 23 (bottom)

Spot 11, PSF shape of bead image at ±200 nm

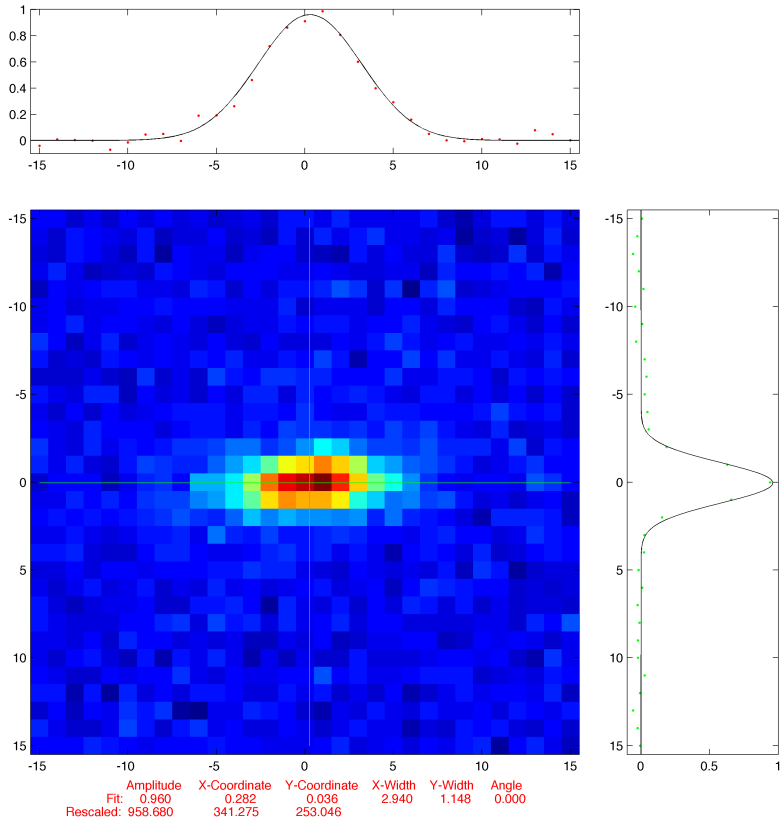

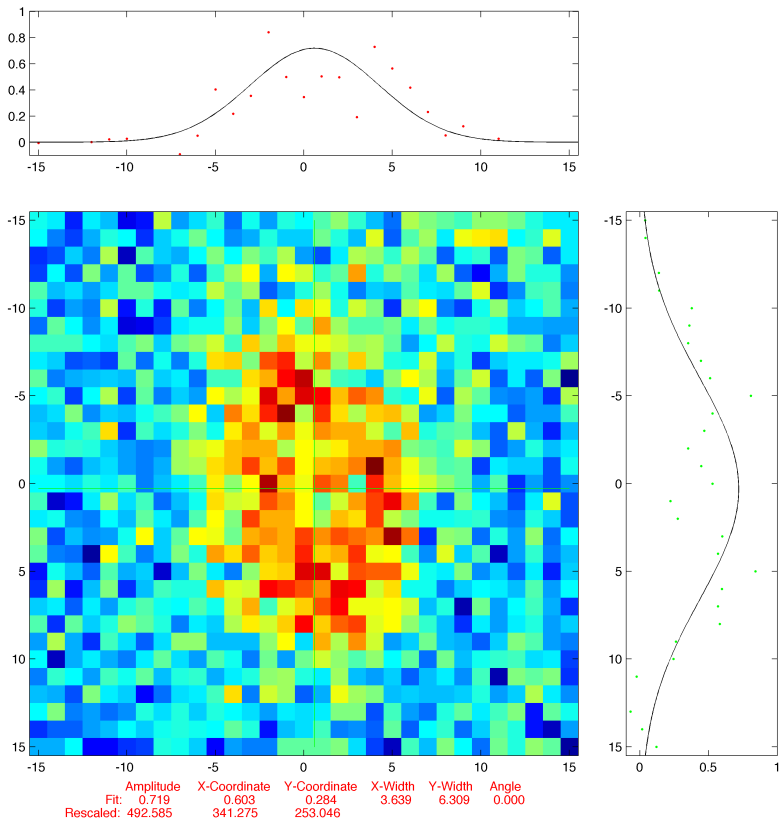

Figures 24 (top) and 25 (bottom)

Spot 11, PSF shape of bead image at ±600 nm

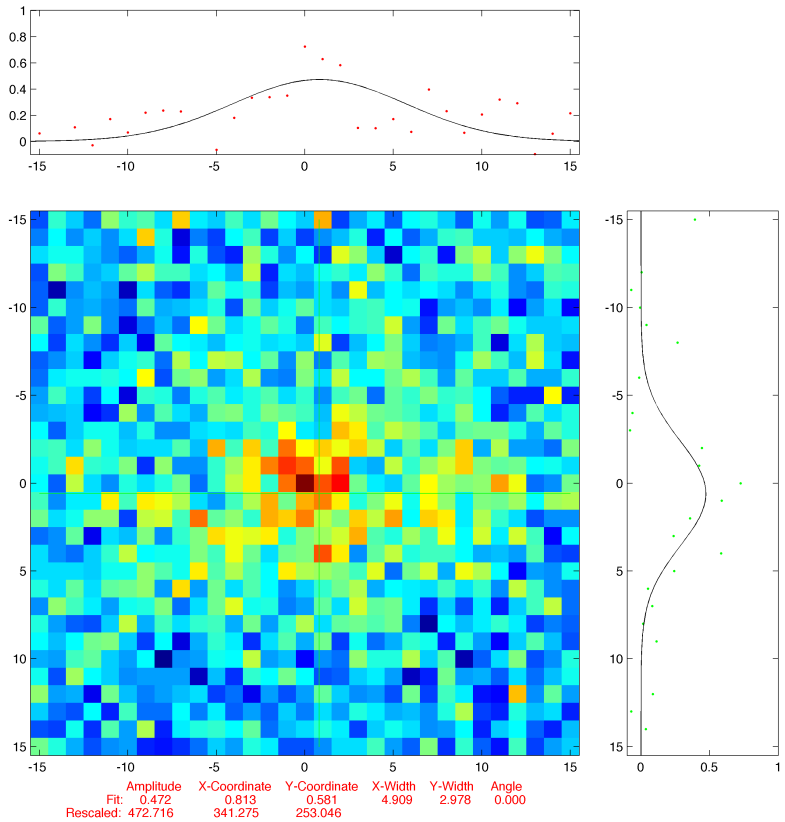

As has been alluded to earlier, the most important metrics to determine a fluorophore's offset from the focal plane are the fitted Gaussian's width and height and the ratio σ_x/σ_y that has a value larger than 1 if the fluorophore is behind the focal plane and less than one if it is in front of it. Given a robust way of discriminating between useful measurements and non-converging data, this gives a very good method of finding the axial position of a spot.

The first step is towards determining if a fit is good or not is to consider the σ-value. If it is smaller than 1, the value can be safely discarded as it is known from the calibration images that the minimal measured width in either direction is always larger than 1: 1.08 in the *y*-direction and 1.34 in the *x*-direction.

The next step is to discard all fits that has a σ-value larger than 6.37. This value is chosen as it produces a Full Width at Half Maximum (FWHM) of 15 pixels, half the width of the ROI.

$$\mathrm{FWHM} = 2 \cdot (2\log(2))^{1/2} \cdot \sigma_{x,y} \tag{10}$$

This value also ties in with the largest Gaussian that can be reliably fitted in the *y*-direction.

To create calibration curves, image stacks of bead samples were recorded at varying axial offset and all spots that were from single beads and could be fitted alone in a 31 by 31 pixel ROI were considered. The *z*-levels were spaced in 100 nm intervals over 2 μm total displacement. For every level, the expectation is that the imaged spots should all have the same shape as they are the same size and on the same distance from the focal plane. The median of this data and ±1 standard deviation error bounds is shown in figure 26 (every point contains 20 spots, analysed at every *z*-position). The calibration curves are the untouched median widths in either *x* or *y* direction. Note the parabolic

shape. The shape is described by the defocusing curve mentioned earlier, in either direction:

$$\sigma_{x,y}(z) = \sigma_0 \sqrt{1 + \left(\frac{z-c}{d}\right)^2 + A\left(\frac{z-c}{d}\right)^3 + B\left(\frac{z-c}{d}\right)^4} \tag{11}$$

In equation (11) σ_0 is the width of the point spread function when the fluorophore is located in the focal plane, *d* is the focus level, i.e. roughly 1.5 μm in the spot 11 example presented here, and finally *c* gives the discrepancy between the focal planes in the *x* or *y* direction and the average focal plane. The quantity *c* is approximated to 0 μm as the system is designed to have co-localisation of the planar focal planes when $z = 0$ μm. The two coefficients *A* and *B* are higher order terms introduced by imperfections in the optical path. Assuming these contributions are small, a second-degree polynomial was fitted to the medians of the *x* and *y* components.

When the displacement is large, the number of divergent spot fits is also large and the error consequently becomes large. To decide the cut-off levels, the fitted widths are considered. Coming from negative displacement, the error along both axes drop sharply at ~-0.6 μm. The error drops below 2 pixels along the *y*-axis from a level around 4 pixels and below 1 pixel along the *x*-axis from a level around 2 pixels, (see figure 27). This is chosen as the lowest allowed starting point for the fit and is also the first point where $\sigma_y < 6.37$ (the reason why fits to spots that give widths larger than this size are discarded). The actual start and end points on either axis were then selected so that the summed absolute difference between the median and the model is minimised and the number of included levels was maximised while still keeping the fit within one standard deviation. This was done for the *y*-axis first and *x*-axis followed when the *y*-axis endpoints had been determined.

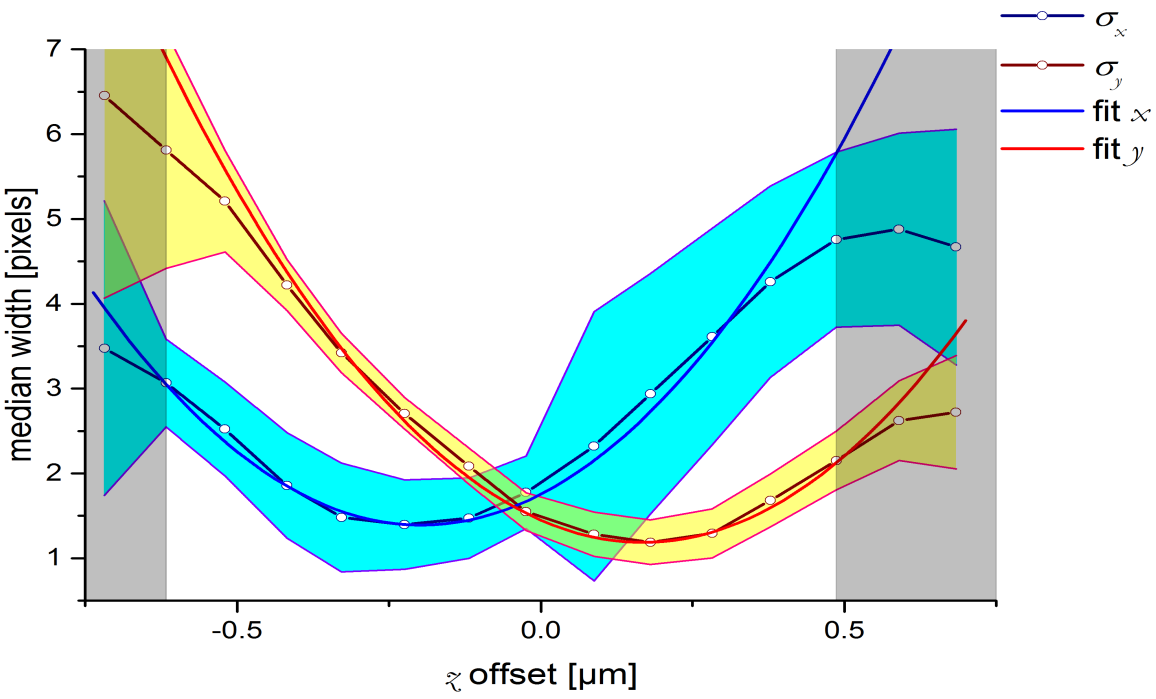

Figure 26 – Calibration curves of σ_x and σ_y as a function of z-offset with 1 standard deviation error bounds.
The second-degree polynomial fits are also shown.
The shaded areas contain combinations that cannot be used.

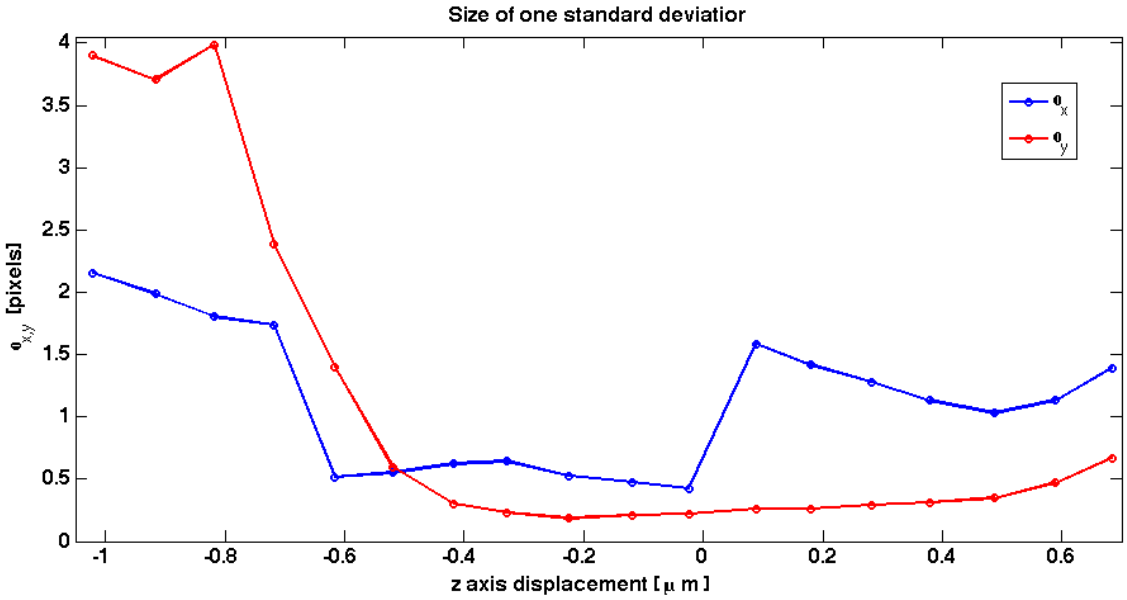

Figure 27 – Size of one standard deviation at varying axial displacement

Figure 28 shows the calibration curve, σ_x/σ_y as a function of axial displacement.

The next step is plotting the ratio of the median widths and heights σ_x/σ_y against the offset, as measured by the feedback system on the nano-piezo stage. The ratio can be used to determine which side of the focal plane a spot is located; a spot located in the symmetry plane has a ratio of 1, see figures 21 and 26. Note how the σ_x/σ_y curve has a very flat appearance and even an inflection point when a spot has a negative displacement. However the fact that the ratio is below 0, this can be used as a flag to use the raw σ_y to encode the axial offset. As the ratio grows above 1, itself can be used as a position reporter.

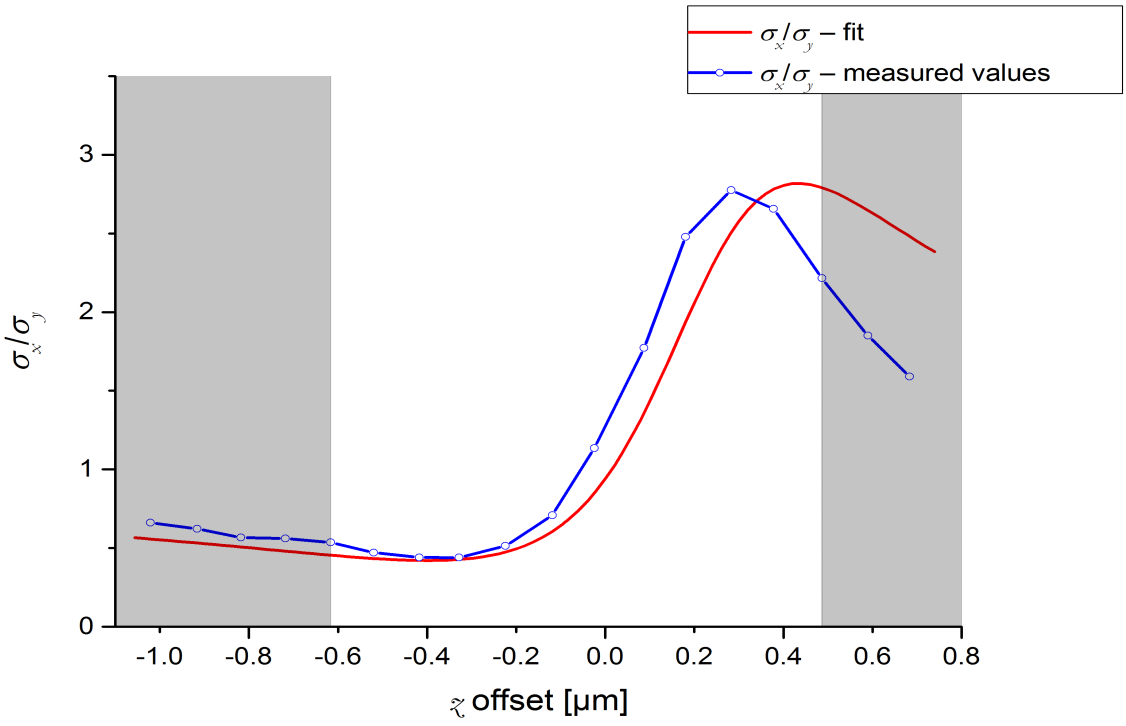

Figure 28 – The calibration curve σ_x/σ_y. The blue curve is constructed from measurements and the symmetry point is located at 0 µm. The red curve is constructed from the polynomial fits (see figure 26). The shaded areas cover data points that cannot be used.

Figure 29 shows an attempted Gaussian fit to a spot in the shaded region. It is clearly shown how the very low signal to noise ratio in this regime and the fact that the spot fills most of the ROI considered makes MATLAB's least-squares algorithm (`lsqcurvefit(...)`) fail to converge and the result is nonsensical values. Both rejection criteria are actually fulfilled here: σ_y<1 *and* $\sigma_x > 6.37$.

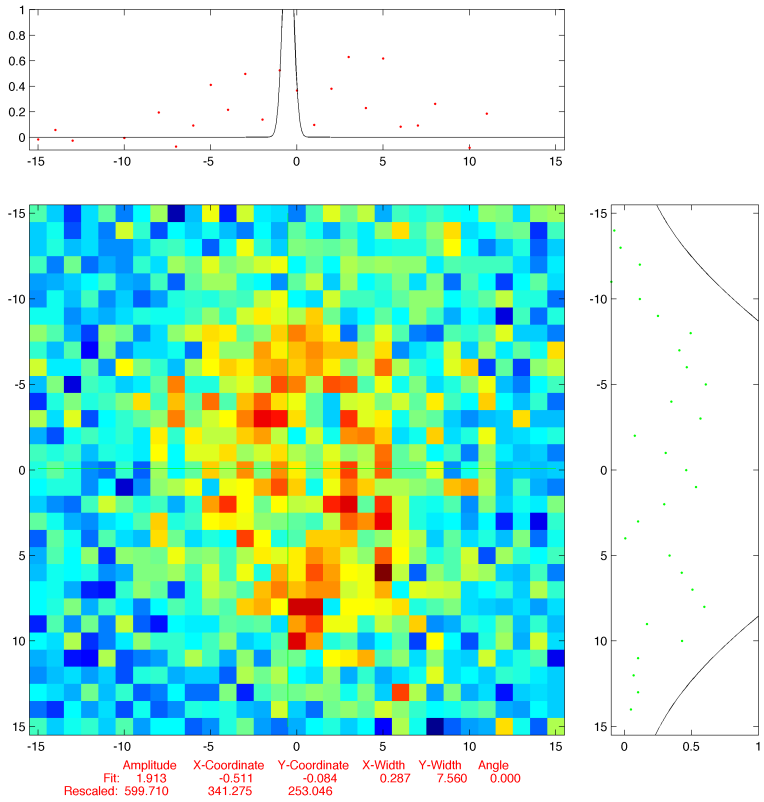

Figure 29 – Failed fitting

Choosing the correct cut-off levels is crucial to get accurate z level estimates and ultimately the limiting factor regarding the recognisable axial displacement.

As mentioned before the measured widths for levels 1 to 6 corresponding to displacements of -600 nm and below have large to extremely large spreads and cannot

be considered reliable. Displacements greater than +500 nm (levels 18 and above) also show a deviation from the model and are similarly considered unreliable.

The chosen cut-offs at 50±550 nm work well as in the *y*-direction the Gaussian fit starts failing to converge after this level and in the *x*-direction the fit starts to trail off in elongation and the errors grow. The bounds in figure 26 are ±1 standard deviation which is ~0.3 pixels. This compared to the median elongation between two levels, which is ~0.8 pixels/100 nm giving an approximate *z*-position error of 37.5 nm.

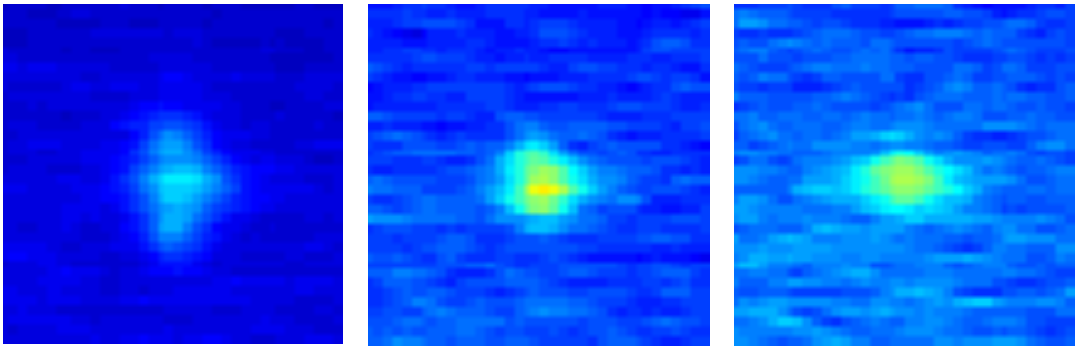

Figure 30 – YPet tagged focus in *Escherichia coli* at three levels. The image on the left hand side is 470 nm below the centre image and the image on the right hand side is 410 nm above it. The spot consists of no more than three YPet molecules.

8 Conclusions and Future Development

The microscope system I built as a part of the work I have conducted in Oxford, has been shown to be able to image and find diffraction limited spots, using primarily light from 100 nm fluorescent beads as source. Further has been shown that small clusters of three molecules of YPet in live *Escherichia coli* can reliably be detected and pinpointed.

In the future more advanced microfluidic flow-channels based on designs from our collaborators in Gothenburg, Groningen and Zürich will be used in order to deliver fresh cells in front of the objective lens, pin them down and expose them to varying environment in order to study dynamic behaviour under varying conditions. The environment can be changed between high and low glucose conditions. An alternate environment containing inhibitors for the targeted proteins can be introduced. An extension of the experiments that could possibly prove possible is to keep a set of cells for several generations using methods such as e.g. integrated micro-pads. A microfluidic channel type featuring micro-pads has been developed in Groningen and may be used in the future for.

Microscope developments that are being considered are different approaches to PSF shaping such as double-helix PSFs, other super-resolution techniques and illumination options such as e.g. TIRF-mode. These are all considered for inclusion in a future system as modules. One illumination mode that is being designed and will be implemented after the move of the equipment to York is a FRAP path. This is an alternate light path for the excitation light that is to be integrated into the existing excitation module. Light in this path will be focussed to a diffraction-limited spot that

can be used for localised pre-bleaching and Fluorescence Recovery After Photobleaching (FRAP).

The limitations of the camera hardware will also need to be addressed. To image dynamical processes a high speed kinetic series will be needed. Aiming for 200 frames per second some sacrifices on the image size will need to be made. For higher speeds the frame needs to be cropped to a narrower Region Of Interest (ROI) to reach a full 200 fps for back to back imaging at 5 ms per frame. This is what is needed in the next step that will be implemented in York for use on live yeast.

A. Appendix: Software Flowcharts (Source Code)

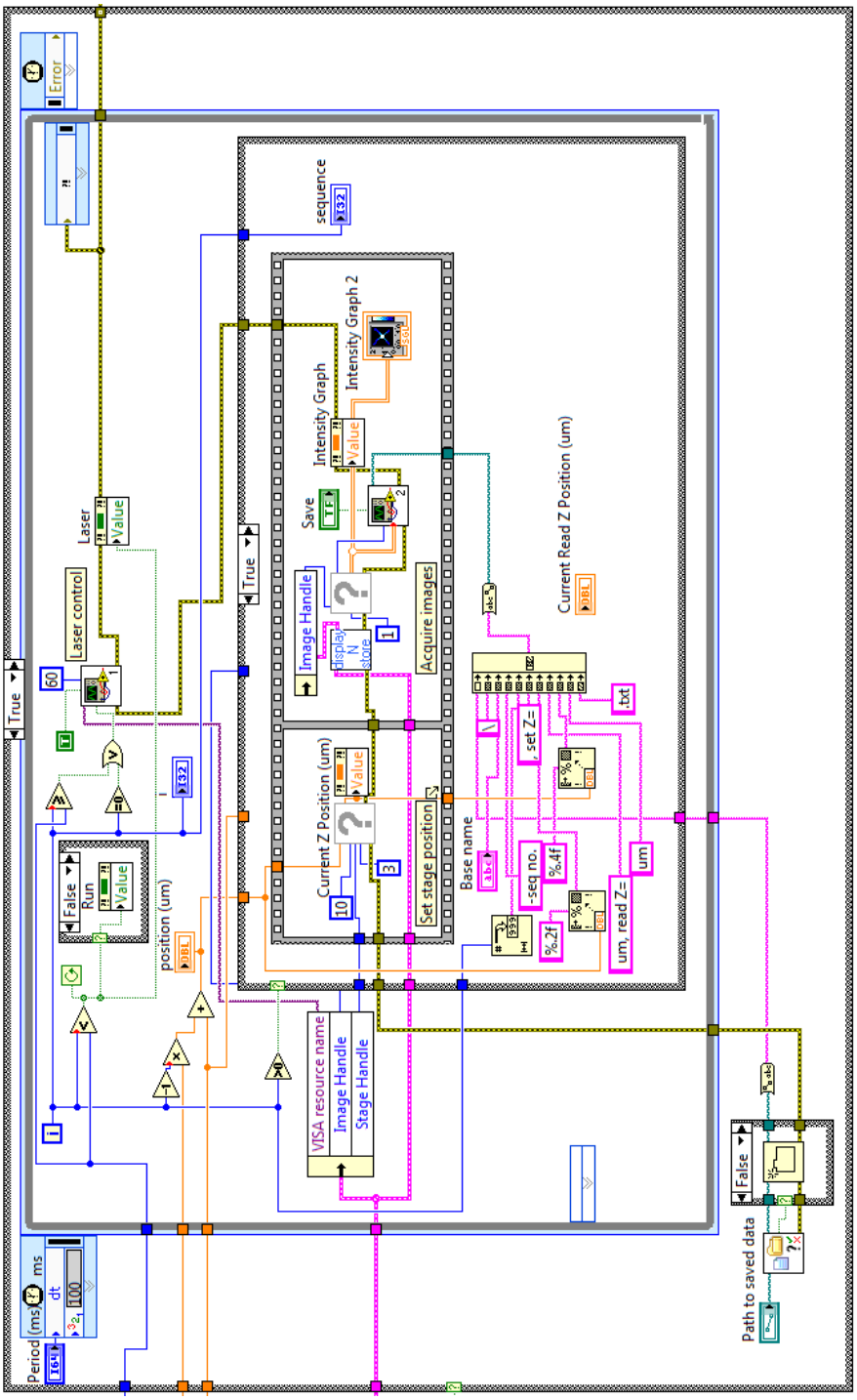

Figure A:1 – Acquisition and stage (z-stack) control loop

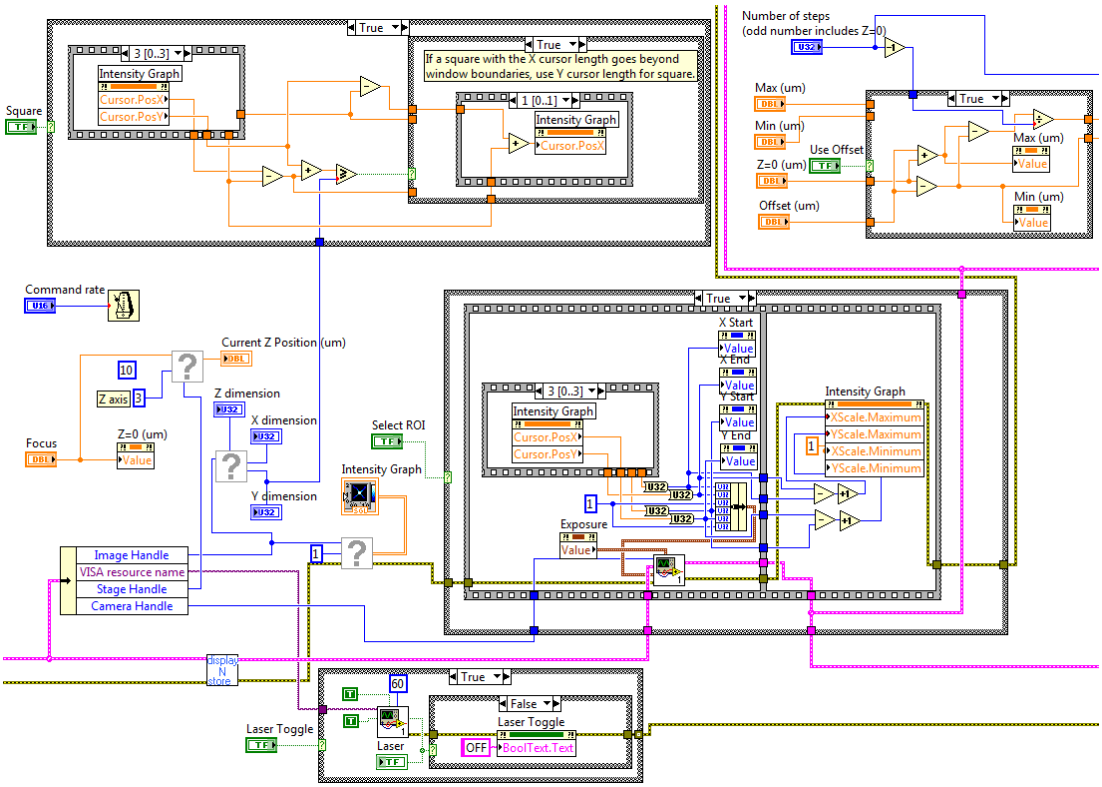

Figure A:2 – Initial setup on start

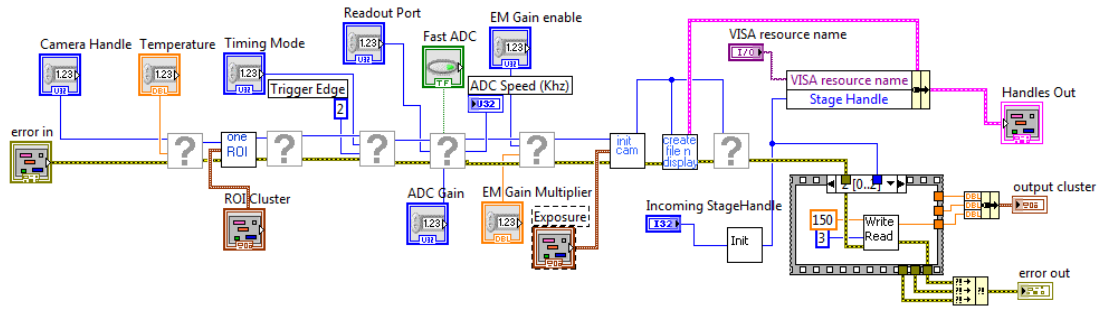

Figure A:3 – Camera initialisation with all parameters present

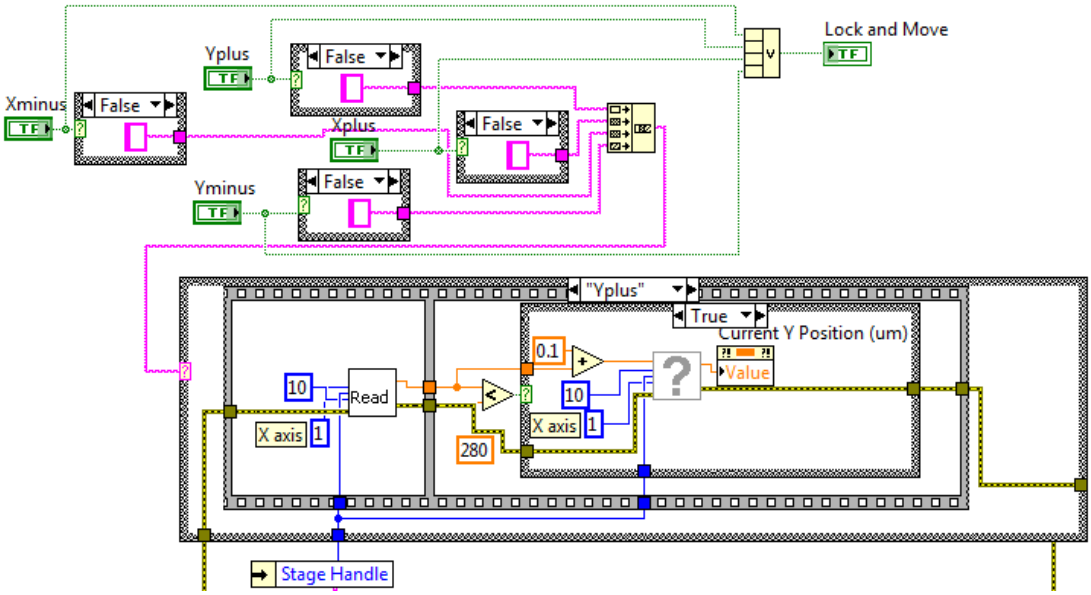

Figure A:4 – Stage positioning (used for fine-tuning of position and focussing)

B. Mandatory Software License Acknowledgements

Gaussian fitting software by Gero Nootz

Copyright (c) 2012, Gero Nootz

All rights reserved.

Redistribution and use in source and binary forms, with or without modification, are permitted provided that the following conditions are met:

* Redistributions of source code must retain the above copyright notice, this list of conditions and the following disclaimer.
* Redistributions in binary form must reproduce the above copyright notice, this list of conditions and the following disclaimer in the documentation and/or other materials provided with the distribution

THIS SOFTWARE IS PROVIDED BY THE COPYRIGHT HOLDERS AND CONTRIBUTORS "AS IS" AND ANY EXPRESS OR IMPLIED WARRANTIES, INCLUDING, BUT NOT LIMITED TO, THE IMPLIED WARRANTIES OF MERCHANTABILITY AND FITNESS FOR A PARTICULAR PURPOSE ARE DISCLAIMED. IN NO EVENT SHALL THE COPYRIGHT OWNER OR CONTRIBUTORS BE LIABLE FOR ANY DIRECT, INDIRECT, INCIDENTAL, SPECIAL, EXEMPLARY, OR CONSEQUENTIAL DAMAGES (INCLUDING,

BUT NOT LIMITED TO, PROCUREMENT OF SUBSTITUTE GOODS OR SERVICES; LOSS OF USE, DATA, OR PROFITS; OR BUSINESS INTERRUPTION) HOWEVER CAUSED AND ON ANY THEORY OF LIABILITY, WHETHER IN CONTRACT, STRICT LIABILITY, OR TORT (INCLUDING NEGLIGENCE OR OTHERWISE) ARISING IN ANY WAY OUT OF THE USE OF THIS SOFTWARE, EVEN IF ADVISED OF THE POSSIBILITY OF SUCH DAMAGE.

Bibliography

Badieirostami, M. et al., 2010. Three-dimensional localization precision of the double-helix point spread function versus astigmatism and biplane. *Applied physics letters*, 97(16), p.161103.

Betzig, E. et al., 2006. Imaging intracellular fluorescent proteins at nanometer resolution. *Science (New York, N.Y.)*, 313(2006), pp.1642–1645.

Fischer, R.E., Tadic-Galeb, B. & Yoder, P.R., 2008. *Optical System Design* Second edi., McGraw-Hill.

Harriman, O.L.J., 2013. *A System-Level Approach to Single-Molecule Live-Cell Fluorescence Microscopy*. Hertford College, University of Oxford.

Hartwell, L.H. et al., 1999. From molecular to modular cell biology. *Nature*, 402(6761 Suppl), pp.C47–C52.

Hedlund, E., 2011. *Construction of a Scanning Laser Confocal Fluorescence Microscope System for Single Molecule Detection and Spectroscopy*. Lund University.

Hess, S.T., Girirajan, T.P.K. & Mason, M.D., 2006. Ultra-High Resolution Imaging by Fluorescence Photoactivation Localization Microscopy. *Biophysical Journal*, 91(11), pp.4258–4272.

Huang, B. et al., 2008. Three-dimensional super-resolution imaging by stochastic optical reconstruction microscopy. *Science (New York, N.Y.)*, 319(5864), pp.810–813.

Juette, M.F. et al., 2008. Three-dimensional sub–100 nm resolution fluorescence microscopy of thick samples. *Nature Methods*, 5(6), pp.527–529.

Kao, H.P. & Verkman, a S., 1994. Tracking of single fluorescent particles in three dimensions: use of cylindrical optics to encode particle position. *Biophysical journal*, 67(3), pp.1291–1300.

Leake, M.C., 2013. *Single-Molecule Cellular Biophysics* First edit., Oxford: Cambridge University Press.

Lew, M.D. et al., 2011. Corkscrew point spread function for far-field three-dimensional nanoscale localization of pointlike objects. *Optics letters*, 36(2), pp.202–204.

Llorente-Garcia, I. et al., 2014. Single-molecule in vivo imaging of bacterial respiratory complexes indicates delocalized oxidative phosphorylation. *Biochimica et Biophysica Acta (BBA) - Bioenergetics*, 1837(6), pp.811–824.

Michalet, X. & Weiss, S., 2002. Single-molecule spectroscopy and microscopy. , 3, pp.619–644.

Ormö, M. et al., 1996. Crystal Structure of the Aequorea victoria Green Fluorescent Protein. *Science*, 273, pp.1392–1395.

Pavani, S.R.P. et al., 2009. imaging beyond the diffraction limit by using a double-helix point spread function. , 106(9).

Pavani, S.R.P. & Piestun, R., 2008. High-efficiency rotating point spread functions. *Optics Express*, 16(5), pp.3484-3489.

Plank, M., Wadhams, G.H. & Leake, M.C., 2009. Millisecond timescale slimfield imaging and automated quantification of single fluorescent protein molecules for use in probing complex biological processes. *Integrative biology : quantitative biosciences from nano to macro*, 1(10), pp.602–612.

Prasher, D.C. et al., 1992. Primary structure of the Aequorea victoria green-fluorescent protein. *Gene*, 111(2), pp.229–233.

Rees, E.J. et al., 2012. Blind assessment of localisation microscope image resolution. *Optical Nanoscopy*, 1(1).

Reyes-Lamothe, R., Sherratt, D.J. & Leake, M.C., 2010. Stoichiometry and architecture of active DNA replication machinery in Escherichia coli. *Science (New York, N.Y.)*, 328(5977), pp.498–501.

Rust, M.J., Bates, M. & Zhuang, X., 2006. Sub-diffraction-limit imaging by stochastic optical reconstruction microscopy (STORM). *Nature methods*, 3(10), pp.793–795.

Saito, H., 2010. Regulation of cross-talk in yeast MAPK signaling pathways. *Current opinion in microbiology*, 13(6), pp.677–683.

Shaner, N.C., Steinbach, P. a & Tsien, R.Y., 2005. A guide to choosing fluorescent proteins. *Nature methods*, 2(12), pp.905–909.

Shashkova, S., Welkenhuysen, N. & Hohmann, S., 2015. Molecular communication: crosstalk between the Snf1 and other signaling pathways. *FEMS Yeast Research*, 15(4)

Shimomura, O., Johnson, F.H. & Saiga, Y., 1962. Extraction, purification and properties of aequorin, a bioluminescent protein from the luminous hydromedusan, Aequorea. *Journal of cellular and comparative physiology*, 59(165), pp.223–239.

Siso-Nadal, F. et al., 2009. Cross-Talk between Signaling Pathways Can Generate Robust Oscillations in Calcium and cAMP. *PLoS ONE*, 4(10), p.e7189.

Thompson, R.E., Larson, D.R. & Webb, W.W., 2002. Precise Nanometer Localization Analysis for Individual Fluorescent Probes. *Biophysical Journal*, 82(5), pp.2775–2783.

Tsien, R.Y., 1998. The green fluorescent protein. *Annual Review of Biochemistry*, (67), pp.509–544.

Webb, R.H., 1996. Confocal optical microscopy. *Reports on Progress in Physics*, 59(3), pp.427–471.

Wegerhoff, R., Weidlich, O. & Kassens, M., 2007. Basics of light microscopy and imaging L. Feldmann, ed. *Imaging & Microscopy*.